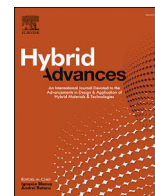# Study of spatial organisation of magnetic field directed gold-pickering-ferrofluid-nanoemulsion in spin coated film.

OKPOZO, P. and PANCHOLI, K.

2023

Study of spatial organisation of magnetic field directed gold-pickering-ferrofluid-nanoemulsion in spin coated film

Paul Okpozo [a], Ketan Pancholi [a,b,*]

[a] School of Engineering, Robert Gordon University, Aberdeen, AB10 7GJ, United Kingdom
[b] Advanced Materials Group, School of Engineering, Robert Gordon University, Aberdeen, AB10 7GJ, United Kingdom

ARTICLE INFO	ABSTRACT
	The magnetic field directed self-assembly of the nanoparticles is cheap, fast and easy method to prepare the patterned thin film useful for various applications. However, the dipole-dipole interaction between nanoparticles at the interface generates the rough-edged patterns even at microscale causing the excess optical scattering making it unsuitable for the optical applications. In this work, the magnetic field was applied during the spin coating of the Polyethylene glycol 40S (PEG) capped Gold-Pickering ferrofluid nanoemulsion (PEG-C-GM-FF) dispersed in aqueous Polyvinyl alcohol (PVA) solution with different viscosities. Optimised combination of spinning speed and magnetic field strength was achieved to prepare the film with the straight chains of PEG-C-GM-FF required for the optical applications. It is a quick, cost-effective, non-intrusive and simple method for achieving a thin layered array of chains with tuneable gaps between them. The image analysis revealed that the Full Width Half Maximum (FWHM) representing the PEG-C-GM-FF chain spatial density across the substrate for each aqueous phase viscosity decreases with the increase in the spin speeds at constant magnetic field strength. The FTIR (Fourier Transformed Infrared Spectroscopy) of the patterned thin film showed that the intensity of the 2927 cm^{-1} vibrational band corresponding to CH bond in PVA was seen to be linearly increasing with the spatial density of the PEG-C-GM-FF chains. In comparison to the gold strip patterns printed with the nanolithography technique; the magnetically aligned array of PEG-C-GM-FF showed a potential for preparing photonic antenna suitable for enhancing the optical absorption and detect low concentration analyte.

1. Introduction

The self-assembly organisation of colloids into long-range two- or three-dimensional (2D/3D) patterns on substrates offers an opportunity to exploit its physical and chemical characteristics in many applications [1]. Mainly photonics antenna are made using lithography, however, in this work, it is proposed that the magnetically directed patterning can be used to produce photonics antenna at lower cost. The conventional top-down processes of nanofabrication like electron beam, ion beam, and UV lithography are expensive as well as complicated to implement, thus incentivising the development of less expensive but precise parallel techniques such as the self-assembly of colloidal particles [2,3]. The controlled assembly of colloidal nanoparticles over a long area can easily be achieved using several techniques like drop casting, Langmuir-Blodgett, gas-liquid interface, sedimentation, dip coating, spin coating, electrophoretic deposition, ink-jet printing, spray coating, etc. [4–12]; however, the degree of control in ordering the colloidal particles

in terms of gaps, spacing, layering formation and overall interparticle interaction requires controlling the balance of forces such as; Van der Waals, electrostatic interaction, capillary forces, stearic effect, magnetic attraction [3,13,14]. Amongst several of the highlighted parallel techniques aligns the colloidal particles in a monolayer or hierarchical hexagonal ensemble [15–17]. The spin coating method is simple to implement and forms a thin monolayered optical band crystal units of polystyrene spheres within a fraction of a minute [18,19]. To improve the flexibility of the spin coating technique, several methods has been applied to break the conventional form of the hexagonal alignment pattern by setting up physical templates and non-intrusive stimulation forces. For example, the combination of spin coating and templated groves [20,21], Spin coating and electric field [22] as well as spin coating and magnetic field [23] have already been used to form the ordered spherical nanoparticles. Hypothetically, the combination of spin coating with magnetic field has an ability to create a thin layered chain-like array type morphology. However, previous investigations utilized magnetic

polystyrene nanoparticles dispersed in an alcohol solvent yielding a disordered (non-conventional array pattern) distribution [24–28]. The use of the Helmholtz coil system in such method increased the interaction between colloidal particles and the axial vector component of magnetic flux field as well the radial vector component due to the centrifugally driven fluid and the spinning motion of the substrate leading to particles experiencing flux switching. In this work, a Helmholtz coil was replaced by the permanent magnet by attaching it to the base supporting the substrate to mitigate the flux switching problem. To prepare an ordered array of the gold nanoparticles, the gold nanoparticles were adsorbed on to the ferrofluid droplets due to its excellent magnetic flexibility in the form of the Fe_3O_4 experiencing both Néel and Brownian motion [29], thereby forging the easy alignment of droplets and translational formation towards the direction of the magnetic field [30]. The oil-based dispersant of the ferrofluid can serve as the medium for organising gold nanoparticles at its interface with water in the form of a pickering emulsion [31]. The combination of nano-emulsion self-assembly and long-range ordered magnetic field induced assembly can bridge the gap in the high throughput fabrication method capable of achieving the high ordered resolution for large area coverage. Use of PVA solution also ensured the maintenance of the structure of the PEG-C-GM-FF chain array after drying. The concentration of the PVA and spin speed dictated the rate of evaporation and drying of the polymer, as well as the film thickness. It is predicted that the inertia force of the aqueous PVA due to spinning would contend with the magnetic force on Pickering nano-emulsion droplets to control the distribution of the PEG-C-GM-FF chains across the substrate. Since PVA has a refractive index of 1.43 between electromagnetic wavelength bands of 300 nm–800 nm [32], the pattern would be easy to visually detect and differentiate from the background, especially when gold nanoparticles are present [33,34].

It is hypothesised the array structure of the PEG-C-GM-FF chains would offer local electric field enhancement to vibrational bands of PVA [35,36] due to intra-nanoparticle confinement of infrared waves. Therefore, it envisaged that a low-cost photonics antenna capable of absorbing infrared via Enhanced Infra-red absorption spectroscopy (EIRAS) [37] can be prepared. In this work, EIRAS in the transmission mode was performed on arrays of magnetically aligned chains of PEG-C-GM-FF to see the variability and effectivity of the formed structure on IR absorption of the PVA.

2. Materials and methods

2.1. Materials

Iron powder (fine), Cis-Cyclooctene (Mw 110.2 g/mol), Hydrochloric acid (37% w/w molar concentration), Ammonium Hydroxide (30% wt. Ammonia in water), Hydrogen peroxide (30% w/w in water) Poly Vinyl Alcohol (PVA) (Mw 88000 g/mol), Oleic acid (Mw 282.46 g/mol), Gold (III) chloride (30 wt % in dilute HCl – Mw 339.79 g/mol), Sodium methacrylate (Mw 108.07 g/mol), Polyethylene Glycol 40 Stearate (PEG 40S). All chemical purchases were made from Sigma Aldrich. DI water with 18 MΩ resistivity, Whatman glass microfibre filter paper (GF/A), plain microscopic soda lime glass slides – 72 mm × 24.5 mm X 1 mm (Agar Scientific).

2.2. Equipment

SCS™ 6800 spin coater, 3 mm × 3 mm X 3 mm square Neodymium Magnets purchased from First4magnets® UK, VTSYIQI® probe type gaussmeter with measurement scope from 0 to 200 mT–~2000 mT (1 mT = 10Gs), resolution of 0.1 mT (accuracy 1%), and operating temperatures −10 °C–40 °C, Olympus® BX41 Darkfield microscope, Quanta 650 FEG Scanning Electron Microscope, Thermo Scientific™Nicolet™iN™ 10 infra-red microscope.

2.3. Methods

2.3.1. Gold pickering ferrofluid preparation

20g of iron powder was dissolved in a solution of 100 ml deionized water 18.2 MΩ-cm resistivity and 100 ml of Hydrochloric acid that formed iron (II) chloride ($FeCl_2$). The solution was split into two and one of them was oxidized to iron (III) chloride ($FeCl_3$) after exposure to air/oxygen for 48 h. On observing guidelines from other processes described elsewhere [38–40], 2 ml of Iron (II) chloride and 2.5 ml iron (III) chloride were added into 100 ml of deionized water in a beaker being agitated in an ultrasonicator bath operating at 40 kHz frequency at 60 °C. The solution was purged with nitrogen gas to prevent oxidation of iron (II) chloride by air. About 60 ml of Ammonium Hydroxide (NH_4OH) was then added drop-wise into the solution bring the solution pH from ~2 to ~9. Subsequently, the colour of the solution changed from orange to brown, and then finally black indicating complete formation of magnetite (Fe_3O_4) nanoparticles. The magnetic nanoparticles separated by magnetic sedimentation (using permanent magnets) from liquid. Repetition of the washing process several times removed the excess ammonium salts. Separated nanoparticles were dried for characterization. Separately, the ammonium-Oleate (NH_4-Oleate) soap was made by mixing 10 ml of Ammonium Hydroxide and 15g of Oleic acid in 20 ml of deionized water [41]. 8g of the paste was then added into the magnetite suspension, and stirred using a rotor stator for 25 min at 1500 rpm. 8 ml of excess ammonia was added within 1 min during the stirring process. 10 ml of Nitric acid was then added dropwise to form salts with excess ammonium ions and reduce the pH to 7. During this process, ionic exchange took place where NH^+ reacted with the NO_3^- to form ammonium nitrate salt, while the oleic ions interact with the Fe_3O_4 nanoparticles to establish layers of coating for stability. The prepared coated Fe_3O_4 nanoparticles were then precipitated and rinsed several times with iso-propanol (C_3H_8O) and deionized water to remove excess ammonia and ammonium salts, and then allowed to dry in vacuum oven at 45 °C, 10 Pa for 24 h. Since the process was repeated in batches, 1g of oleic acid coated iron oxide (Fe_3O_4) (Fig. S1(a)-Supplementary Information) was separated for characterisation and 5g was dispersed in 7 ml of Cis-Cyclooctene [$(CH_2)_6(CH)_2$] to create the oil-based ferrofluid (Fig. S1(b)-Supplementary Information).

Gold methacrylate was prepared following the process; 0.0196g of Gold (III) Chloride was diluted in 5 ml of deionized water. 0.407g of Sodium methacrylate dissolved in 20 ml of water was prepared. The diluted Gold (III) Chloride was poured into a 100 ml of deionized water boiling at 90 °C while being stirred [42]. 12 ml of dissolved sodium methacrylate was added at once into the boiling solution. The mole ratio between gold ions and methacrylate ions is 1:39. The process was then observed for 15 min as the solution turned from transparent to a red-wine colour (Fig. S1(c) in Supplementary Information) of dispersed colloids. This meant that the free excess acrylic ions established hydrophobic interactions/network with the acrylic ions attached to the gold(Fig. S1(d)-Supplementary Information), to create a double layer/-charge that promoted repulsion and stability of the colloids [42]. After cooling to room temperature (21 °C), 20 µg/ml of PEG 40S solution was added to the gold colloid and allowed to mix in a 200 ml beaker sealed with aluminium foil while using a magnetic stirrer at 500 rpm for 6 h. This was to establish a layer of coating by hydrophobic interaction, thereby making the particle dispersible in water even after modifying the pH [43,44,44a,44b,44c,44d]. The PEG-capped gold Methacrylate (PEG-C-GM) nanoparticles were then separated from solution using a Eppendorf® centrifuge 5418 at 11000 rpm and were rinsed with deionized water. This was repeated four times to remove sodium salts and excess PEG molecules. The final treated particles were left in 15 ml of deionized water until further use. The concentration of the particles in water at this stage was 4.2 ± 0.2 mg/L, the zeta potential and particle sizes for both PEG capped and uncapped are shown in (Fig. S5and S4(a)-Supplementary Information). The TEM image of PEG-Methacrylate capped gold (PEG-C-GM) nanoparticle is shown in (Fig. S2

(b)-Supplementary Information).

4 mL of gold methacrylate colloid solution was dispersed in 20 mL of deionized water and sonicated using sonicator bath for 5 min. 70 μL of ferrofluid was dispersed in the solution by stirring at 800 rpm using a rotor stator for 8 min to create micron sized droplets (~400 μm diameter). Then the pickering emulsion was formed using a probe type MSE® Soniprep 150 ultrasonicator, operated at 10 μm probe amplitude displacement, with a frequency of 20 kHz for 10 min, and a pulsation of 10 s on, 3 s off. The system was kept cool (~19 °C±2 °C) by inserting it into a temperature regulating jacket. The pickering emulsion size was tested using Malvern zeta sizer and the average droplet size after sonication was 600 ± 500 nm and after centrifugation was 330 ± 200 nm, see (Fig. S4-Supplementary Information).

15 ml of emulsion solution was poured into the 6 centrifugal 20 ml tubes and was centrifuged using at a predetermined speed of 1000 rpm for 10 min to reduce degree of polydispersity. The concentration of droplets was increased by placing a 2 T magnet beneath the beaker containing the centrifuged emulsion solution, while the supernatant was carefully decanted. The new mixture was termed Polyethylene glycol coated gold methacrylate Pickering ferrofluid (PEG-C-GM-FF) (Fig. S1(e)-Supplementary Information). At the same time 5 wt%, 3.3 wt %, 1.7 wt%, and 1.3 wt% of aqueous Polyvinyl alcohol (PVA) was prepared by dissolving PVA into DI water and stirred at 200 rpm for 10 [45–48]. The solution was then heated up to 80 °C for 1.5 h to finally obtain a clear viscous liquid.

The concentrated Pickering emulsion was then added into 10 mL of aqueous solution of PVA and stirred at 400 rpm for 1 h using a rotor mixer. Further, all characterisation performed, such as transmission electron microscopy (TEM), dynamic light scattering (DLS), zeta potentials and magnetic hysteresis, are detailed in *Supplementary information (S.1)*.

2.3.2. Thin film preparation

A schematic of the set-up used for preparing the thin film is shown in Fig. 1(a). As seen in Fig. 1 (a), the 3 mm × 3 mm x 3 mm permanent magnet (105 mT) attached securely on the base support was placed on the vacuum chuck such that the top surface of the magnet remained exactly 5 mm below the thin film substrate. The top view of the cuboid magnet location in relation to the top substrate with PEG-C-GM-FF in PVA solution is shown in Fig. 1 (b) while the measured (using VTSYIQI® probe type gaussmeter) radial distribution of the magnetic field (mT) between the centre of the neodymium cuboid magnet (r = 0 m) to the location on the surface of the substrate at r = 0.02 m is shown in Fig. 1 (c). As seen in Fig. 1(c), the magnetic field is not uniform beyond a

millimetre of diameter from the centre of the film or rotation. However, creating an array for permanent magnets with opposite poles placed next to each other can create a uniform magnetic field."

The setup was spun using a SCS™ 6800 spin coating series equipment under variable speed programmed to operate within specified time frame. The time for the process was divided into three sections; the first, an acceleration from 0 rpm to highest speed for 5 s; secondly, a constant top speed for 50 s; and the third, a deceleration for 5 s. Prior to starting the spinning process, 0.5 ml of PEG-C-GM-FF in PVA solution was allowed to settle on the substrate for 60 s. This gave enough time for the PEG-C-GM-FF nanoemulsion droplets to migrate toward the highest magnetic field strength (centre of the magnet at r = 0) and build arrays of the chains due through dipole-dipole interaction. After 60 s of spinning process, it was noticed the thin film had dried, except for thin film emulsions operated at 700 rpm, which dried 2 min after. During the drying of the partly wet sample containing water, the PEG-C-GM-pi-FF chains started dissembling due to removal of magnetic field. Therefore, it was necessary to prepare the thin film at the high spinning speed (in this case, >700 rpm) to maintain the structure of the arrays of the chain even after completion of the spin coating process.

Table 1 summarises the parameters used for preparing patterned thin film in the study. The PEG-C-GM-FF nanoemulsion was dispersed in different concentrations of aqueous PVA (5w/w%, 3.3w/w%, 1.7w/w% and 1.3w/w%) solution following the procedure described in section 2.3.1. The parameters such as aqueous PVA viscosity and spin speed were varied (Table 1) to prepare a patterned films that allowed the observation

Table 1

The relevant physical properties of PVA solution at room temperature and the process parameters used for preparing the thin films in the study.

PVA concentration (w/w%)	Density (kg/m³)	Viscosity mPa.s	Surface Tension (mN/m)	Centrifugal speed (RPM)	Time (sec)
5%	1015	43.2	50.8	700, 1000, 1500, 2000, 2500	60
3.3%	1011	15.2	51.7	700, 1000, 1500, 2000, 2500	60
1.7%	1006	3.2	52.8	700, 1000, 1500, 2000, 2500	60
1.3%	1005	1.9	53.3	700, 1000, 1500, 2000, 2500	60
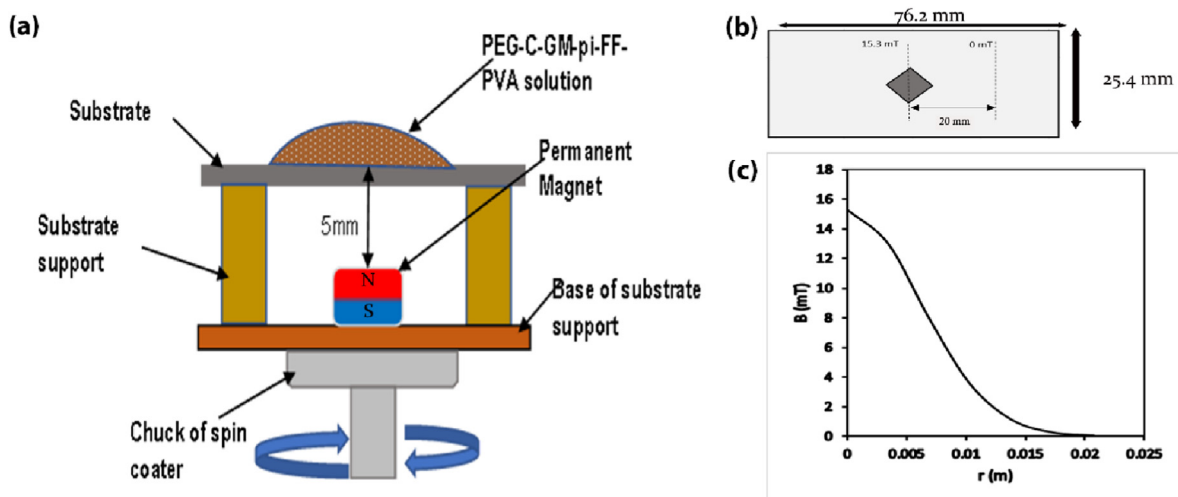
Fig. 1. (a) Schematic of cross-section dimensions of experimental setup with droplet interaction in magnetized ferrofluid-polymer emulsion. (b) Top section showing square magnet single type and radial length of field intensity (c) Radial magnetic field distribution across substrate surface.

of change in morphology of the arrays of the chains present in the film.

2.3.3. Optical microscopy and scanning electron microscopy

Optical images of the patterned thin film were captured using an Olympus® BX41 Darkfield microscope attached with M-plan Achromat MPLN-BD 50X, NA 0.5. All 1920 × 1080 images were obtained with resolution of 0.17 μm/pixel. To observe the change in the density of the chains with respect to the centre of the film (Fig. 2(a)), the spatial location on the film were determined using the vernier scale of the microscope stage and cross-referenced with the spatial density of the chains at that position in microscope images. Furthermore, the film was shifted along the straight line observe the spatial density of the PEG-C-GM-FF chains at different radial locations away from the centre. Darkfield microscopy (Fig. 2(b)) offered a close to binary image showing the nano-emulsion droplets appearing bright in the dark background making it easier to distinguish structure from background. The images were analysed using Image J® tool.

Dried spin coated samples were also imaged using a Quanta 650 FEG SEM to observe the morphology. A low-pressure vacuum of 0.825 Torr, 20 kV accelerating voltage (HV) and working distance of 10±1 μm was used for all point scans depending on the magnification. An example SEM image (Fig. 2(c)) at the high magnification showed the presence of at least two layers of PEG-C-GM-FF nanoemulsion droplet layers.

2.3.4. Image analysis method

Firstly, the darkfield microscopy images of the patterned thin film were converted to binary format causing the pickering droplets to appear as white in the black background. The contrast between the two allowed to identify the number of white pixels in a unit region of interest representing the chain density using the image analysis. The Region of Interest (ROI) on the microscope images was defined by drawing the series of concentric rings of different diameters from the centre of the prepared thin film as seen in Fig. 3 (a&c) and the pixel density between each ring was measured using the image analysis. The gap between each ring was kept in the range of ~20 ± 5 μm. Maximums and integrated density functions in image J® used for determining the pixel density per scan area. Before analysis, the noise was removed from the images by keeping the in-focus white pixels. Further analysis was performed to extract the integrated pixel density for each ROI and generated the density distribution profile at various radial locations on the patterned film.

3. Results and analysis

3.1. Integrated pixel density in region of interest

The example images of two sets of patterned films prepared from PEG-C-GM-FF nanoemulsion in PVA (3.2 mPas) at 700 rpm and 2000 rpm spinning speeds are shown in Fig. 3 a & c. The raw data of the integrated pixel density per area in thin film prepared at 700 rpm and 2000 rpm are included in Supplementary Tables S2 and S3, respectively. The integrated pixel density (IntDen) per unit area of the ROI_1 to ROI_3 was found to be constant (~4080) for the thin film prepared at spinning speed of 2000 rpm or less. However, IntDen per unit area was found to be gradually declining from ROI_4 to ROI_6. These estimated IntDen values per unit area (on y-axis) were plotted against the diameter of each yellow ROI circle (on x-axis) (Fig. 3 (b) & (d)), where the centre of the film (Fig. 2(a))
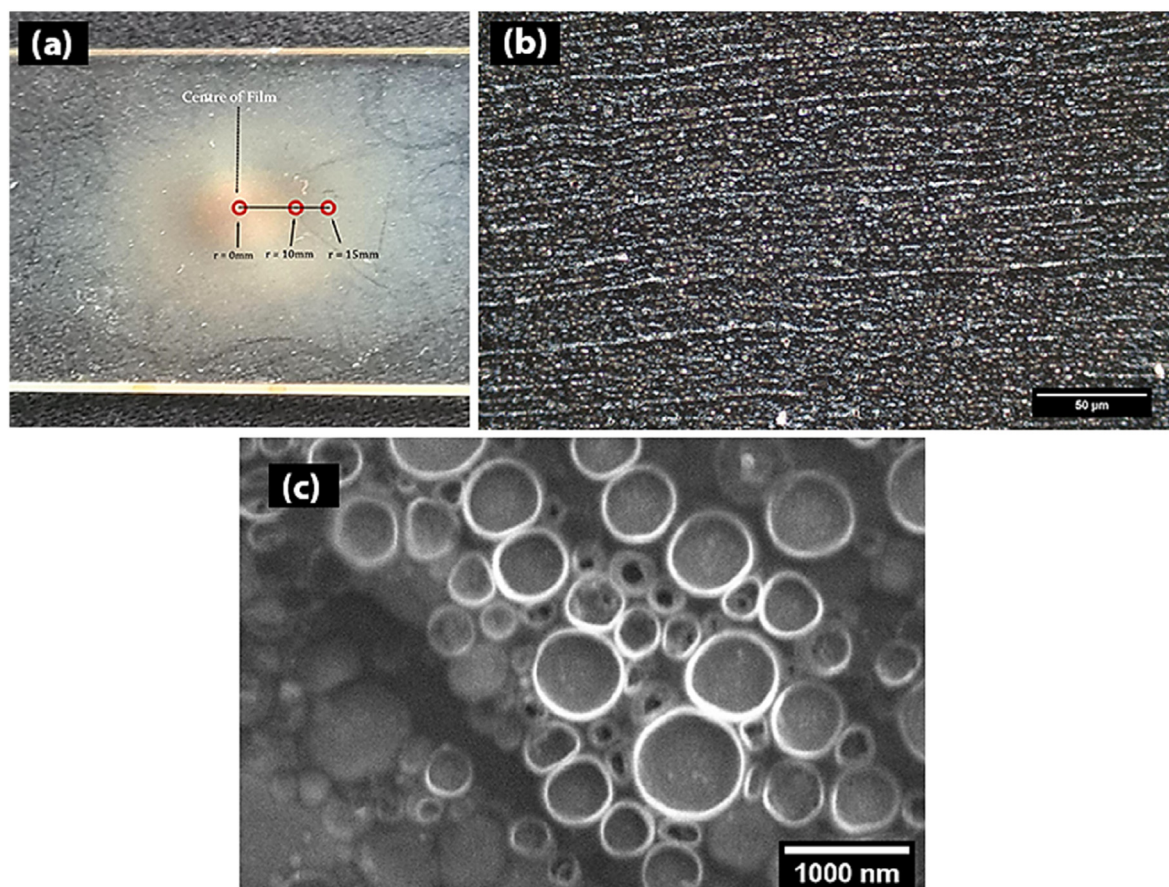
Fig. 2. (a) A typical image of thin film on glass slide and radial location where integrated densities were measured. Each red circle represents the area equivalent to sum of area of ROI_1 to ROI_3 (b) the dark field optical image of structure pattern at r = 14 mm, (c) SEM image of structure at r = 1 mm. All images show the thin film prepared using PEG-C-GM-FF nanoemulsion dispersed in PVA solution of 15.2 mPas viscosity at spin speed of 2000 rpm. (For interpretation of the references to colour in this figure legend, the reader is referred to the Web version of this article.)
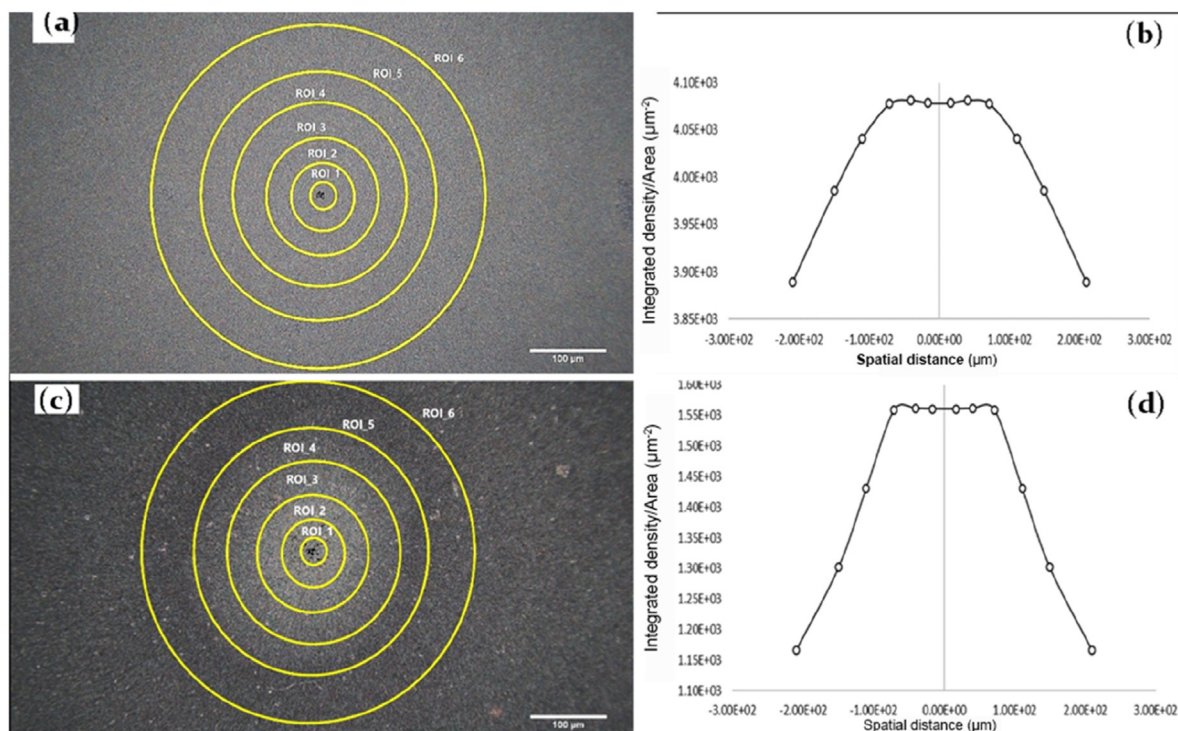
Fig. 3. The representative microscope images of the films prepared by spinning PEG-C-GM-FF nanoemulsion dispersed in PVA solution having viscosity of 3.2 mPas at (a) 700 rpm (c) 2000 rpm. The area between two consecutive yellow circles drawn on both images represent the region of interest (ROI) areas. Variation in the integrated pixel density of each ROI area in relation to diameter of each outer circle of ROI for corresponding images in (a) and (c) are shown in (b) and (d), respectively. The points showing lowest integrated density value in plots in (b) and (d) corresponds to ROI_6. (For interpretation of the references to colour in this figure legend, the reader is referred to the Web version of this article.)

was considered X = 0 μm. All the diameter values right to the centre of the pattern was considered positive whereas the diameter values on left of the centre of the film was negative. The magnetic field of 15.3 mT was constant up to 120 μm radius from the centre of the film as seen in Fig. 1(c).

This profile in Fig. 3(d) represents the PEG-C-GM-FF chain density distribution shown in Fig. 3 (c). On comparing both Fig. 3 (b) and (d) as well as considering the distribution curve peak point at centre- 0 mm, it was observed that the increase in spinning speed from 700 rpm to 2000 rpm caused an increase in a fluid inertia to reduce the film thickness containing PEG-C-GM-FF chain layers by ~160%. The difference between the IntDen at peak of the distribution curve (Fig. 2(b)) and lowest point was 5% for 700 rpm, while it was 35% for 2000 rpm. Meaning, the increased spinning speed increased fluid inertia high enough to effectively overcome the magnetic force on PEG-C-GM-FF nanoemulsion droplets, resulting in reduced chain density close to the centre of the film, thereby forming a steep slope in the profile (Fig. 3(d)). This form of patterned thin film would minimize the contributing effect of hierarchical structures formed by the PEG-C-GM-FF droplets, toward more of spatial chains and gaps distribution. It was observed that the pixel density for ROI_1, 2 and 3 were found to be approximately same, hence, the pixel density for the ROI_3 (1.50×10^4 μm^2), encompassing the area from the centre of the film to the outer boundary of ROI_3 (Fig. 3 (a) & (c)), was only recorded to analyse results for section 3. Since the area range of the thin film to be scanned is 1257 mm^2 (where radius = 20 mm), as well as the field of view covered by the 50X magnification lens along with CCD captured area (~0.35 mm^2), it became logical to capture scanned local points along the radial range of the thin film using ROI_3. Since the area of ROI to be used is the same across, the radial points, the Integrated density (IntDen) was used as the quantification parameter for bright pixel density of PEG-C-GM-FF droplets. The thin film for application purposed should only be utilized up to ROI_3, beyond the pattern formation was found to be random and not considered for further analysis in this work.

3.2. Effect of speed and viscosity on spatial distribution

As seen in Fig. 3, the integrated density was constant from ROI_1 to ROI_3 and hence, the integrated density was calculated for all three ROI at various radial locations from r = 0–18.5 mm and plotted against the radial distance from the centre on the film (Fig. 4). As seen in Fig. 4, the long-range radial distribution profile of PEG-C-GM-FF nanoemulsion droplets was constructed by fitting the integrated densities measured at
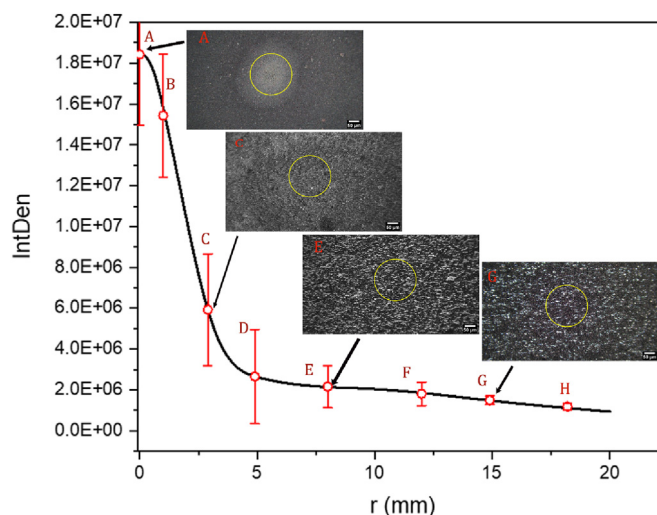
Fig. 4. Plot shows the change in PEG-C-GM-FF nanoemulsion chain density (represented as integrated density [IntDen]) observed at various scanned locations on film processed at 2000 rpm using (from left to right) PEG-C-GM-FF nanoemulsion in aqueous PVA solution (1.7 wt% or 3.2 mPas). The Pseudo-Voigt-1 model fit for [IntDen] using Origin® resulted in an R^2 of 0.9983.

each scanned radial points between r = 0 mm to r = 18.5 mm on film, where each radial point encompassed the area equal to summation of all three ((Fig. 2(a) - from ROI_1 to 3 (1.50×10^4 μm^2). The IntDen was not divided by the region of interest area because it was the same size used for all scanned radial points. An example plot shows the integrated density was found to be highest at centre of the film (probably spinning centre and where magnet is located) and lowest at the location farthest from the centre. The distribution was a half-normal with a higher IntDen at the centre of the film (r = 0 mm). The film was processed using aqueous PVA solution with viscosity of 3.2 mPas, spun at 2500 rpm (Fig. 4).

Similar to Fig. 4, the IntDen representing the PEG-C-GM-FF nanoemulsion chain densities was plotted for all parametric combinations as mentioned in Table 1 and are presented in Fig. 5. The rest of the distributions obtained for films prepared using preselected viscosities and spin speeds related to both Fig. 5 are provided in Supplementary Fig. S6. The change in profile under constant magnetic field was influenced by the viscosities of the PEG-C-GM-FF nanoemulsion in PVA and selected spin speeds.

The profiles in Fig. 5 demonstrate the overall impact of the viscosity on the distribution of IntDen at the same magnetic field strength but for all spinning speed. At centre of the film, the magnetic field trapped the PEG-C-GM-FF nanoemulsion droplets on substrate in high concentration which translated into high IntDen at the centre of the microscope image (corresponding to highest density points in all four subplots in Fig. 5). As

spinning speed increased, the IntDen at the centre reduced in relation to viscosity. The microscope image for the film prepared at highest spinning speed (2500 rpm) using the highest viscosity (43.2 mPas) showed higher integrated density (~6.5×10^7) at centre compared the integrated density (~4×10^7) at centre of the image of film prepared at 2500 rpm using 1.9 mPas viscosity.

The spatial distribution of PEG-C-GM-FF nanoemulsion chains on substrate, a result of the interaction between three parameters, could be captured by measuring the full width half maximum (FWHM) of distribution peak. Increased FWHM values shows the increase in the overall integrated density. The FHWM identifies with the degree of spatial spread of the PEG-C-GM-FF nanoemulsion droplets across the thin film. This was estimated using Gaussian fitting tool in Origin® software. The plot of FWHM vs spin speed (rpm) for each aqueous PVA viscosity is shown in Fig. 6.

The change of FWHM of PEG-C-GM-FF nanoemulsion droplets distribution as speed increased differ for each PVA viscosities. If the viscosity of the PVA solution was increased, the spread of the spatial distribution PEG-C-GM-FF nanoemulsion droplets (FWHM) decreased due to increase in viscous resistance. Viscous drag resulted in reduction in the displacement of the magnetized PEG-C-GM-FF nanoemulsion droplets away from the centre. At the higher spinning speed, the integrated density (Fig. 5) was found to be greater at the radial position of 13 mm ± 0.4 and above compared the lower spin speeds.

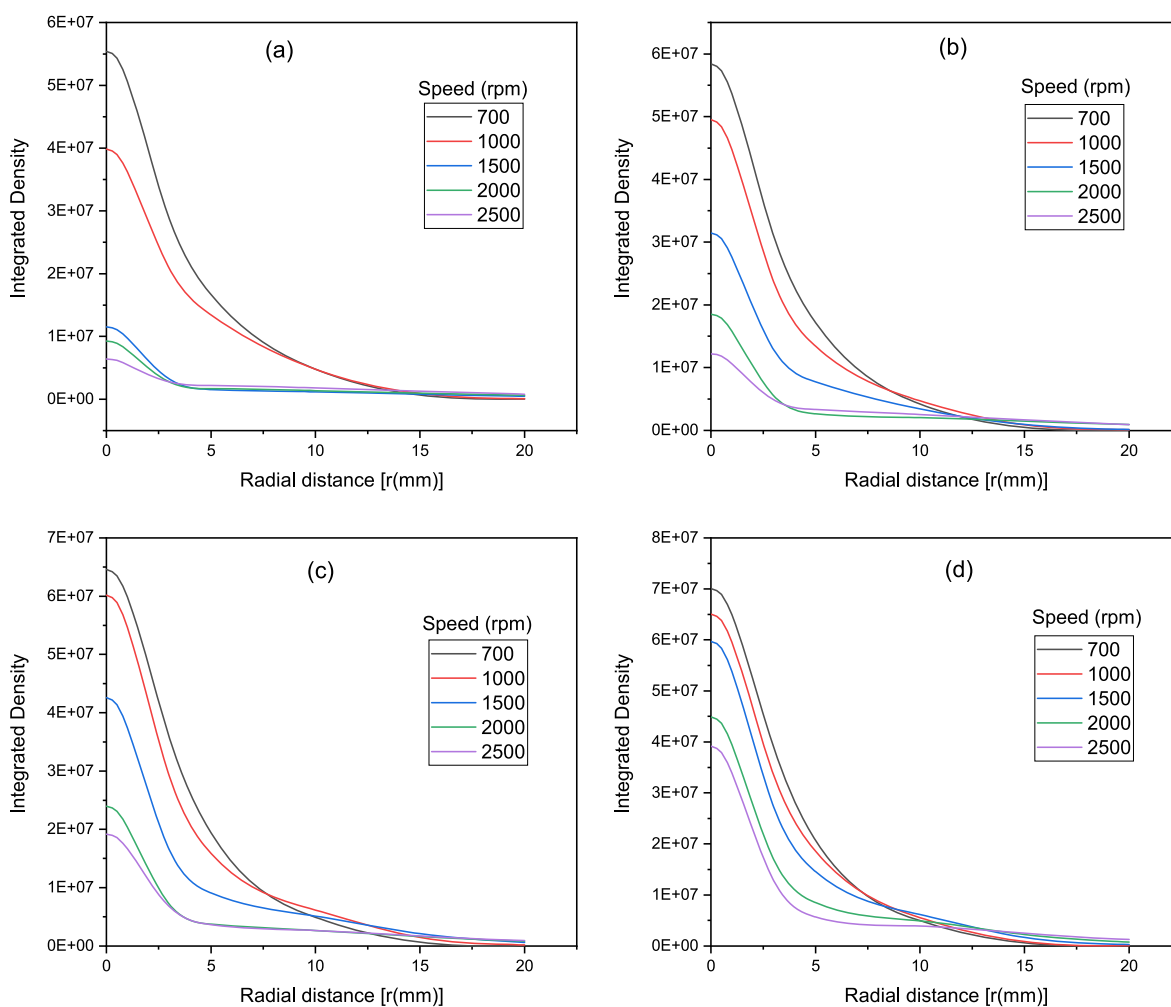This could have happened due to the instability induced wave like

Fig. 5. Gaussian distribution of integrated density of PEG-C-GM-FF chains at various radial locations across thin film prepared by spinning at spin speeds of 700, 1000, 1500, 2000 and 2500 rpm using the PEG-C-GM-FF nanoemulsion in PVA aqueous solution having viscosity; (a) 1.9 mPas, (b) 3.2 mPas, (c) 15.2 mPas and (d) 43.2 mPas.
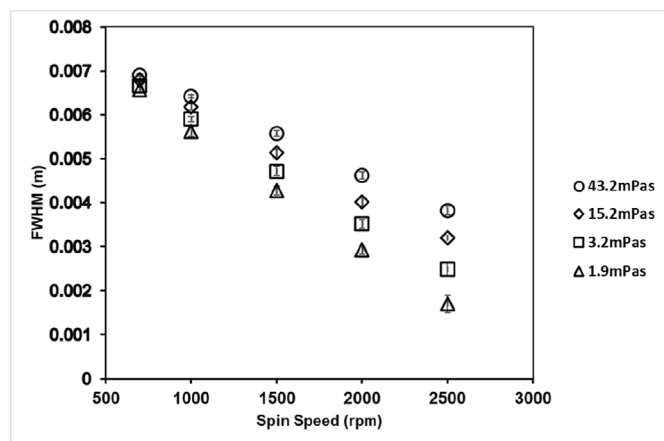
Fig. 6. *The full width half maximum (FWHM) of the distribution peak of* PEG-C-GM-pi-FF *nanoemulsion droplet distribution each PVA of viscosities (1.9 mPas, 3.2 mPas, 15.2 mPas and 43.2 mPas) plotted against spin speed (rpm).*

formation on substrate when it was spun at high rotations. The wave contained comparatively large number of droplets and moved to away from the central region (>1 mm) to farther regions of the substrate. The statistical distribution profile only measured the relative quantity of PEG-C-GM-FF nanoemulsion droplets at specific regions of the substrate [21]. However, the dipole-diploe interaction between PEG-C-GM-FF nano-emulsion droplets in presence of magnetic field established the orders of linear chains and changed the gaps between chains across the thin film [19,22]. Thus, the measured changes would qualitatively relate to the applied magnetic field strength and fluid inertial energy rendering the tunability of the resolution of the chain grating. After observation via images of samples prepared under varying viscosities and spin speeds (see examples through *Supplementary S.2.3*), the preferred configuration selected going forward for thin film nanostructure coating on glass slide was 15.2 mPas PVA viscosity and speed 2000 rpm and above because it gave a better grating profile/pattern.

3.3. Fourier transform infrared absorption

Fourier transform infra-red spectroscopy (FTIR) was performed on the PVA- PEG-C-GM-FF patterned film for label-free characterisation to observe the molecular vibrations related to each constituent of the Pickering emulsion [49,50]. Identifying the spectral signatures corresponding to molecular vibrations helped confirming the presence of remaining chemical/metal constituents and suppression of any peak due to interaction between each constituent with Pickering emulsion [51,52]. Coupling between adjacent nanoparticles is known to increase the IR absorbance and allows detecting molecule at low concentration. The grating structures containing the periodic gold strips also enhances IR absorbance of the molecules adsorbed on the surface through surface lattice resonance and near field coupling [53,54]. Such structures have seen applications as antennas on substrate for surface enhanced infra-red absorption spectroscopy [36,55]. The arrays of PEG-C-GM-FF chains prepared as part of this study, were geometrically imperfect at nanometre scale but could increase the IR absorbance of PVA molecules through iron oxide nanoparticle to gold nanoparticle interaction. To test the hypothesis, the FTIR was performed.

An example of spectra collected at various locations on the thin film nanostructure prepared using 45.2 mPas PVA- PEG-C-GM-FF at spin speed of 1000 rpm is shown in Fig. 7. The spectra in relation to the spatial locations (r (m)) on the PVA- PEG-C-GM-FF film were collected from the centre of the film (r = 0 m) to a farthest position (r = 11 mm).

As seen in Fig. 7, the broad and strong O–H peak at 3350 cm^{-1} is associated with alcohol in PVA [56]. Peaks at 2927 cm^{-1} and 2847 cm^{-1} assigned to the asymmetric and symmetric stretching vibrational
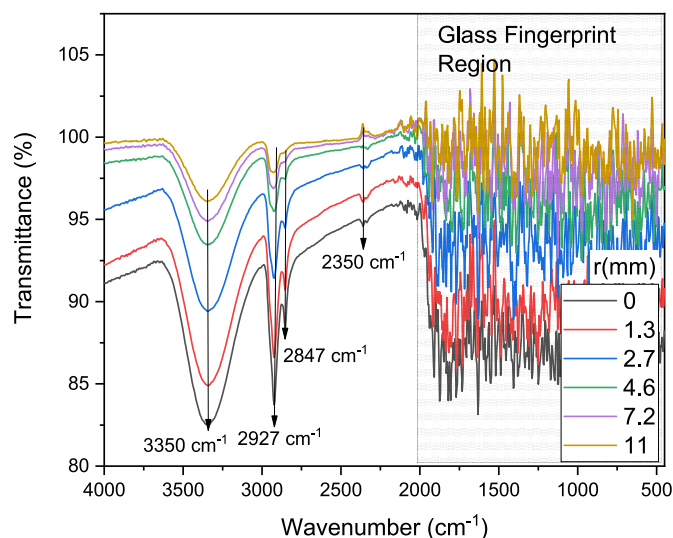

Fig. 7. FTIR spectra of PVA- PEG-C-GM-FF film nanostructure (45.2 mPas PVA-PEG-C-GM-pi-FF at spin speed of 1000 rpm) on glass substrate with different radial position r (mm).

transitions of methylene –CH_2 bond, respectively [57]. The peak at 2350 cm^{-1} is assigned to CO of carbon dioxide [58]. The regions from 1950 cm^{-1} and below appear scattered due to the diffraction limit of infra-red light and the fingerprint region of soda lime glass (substrate) [59,60]. These vibrational modes were excited by infra-red wave in this wavenumber range.

The absorbance intensity of band at 2927 cm^{-1}, calculated using (2-Log(%T)) [61], was monitored by acquiring FTIR spectrum at various radial distances across the film and plotted against the radial distance to observe if there was any correlation between the intensity of the absorbance peak and integrated density of the PEG-C-GM-FF nanoemulsion chains. The typical plots in Fig. 8(a) and (b) shows the FTIR spectra obtained from various radial location on the film prepared by spinning the PEG-C-GM-FF nanoemulsion dispersed in PVA solution with 1.9 mPas viscosity at 700 rpm and 2500 rpm, respectively. The variation in the intensity of the 2927 cm^{-1} peak in relation to the radial locations shown in Fig. 8 (c) and (d) were extracted from Fig. 8 (a) and (b), respectively. The local plasmon charge excitation on the gold nanoparticles with chain and far field excitation between PEG-C-GM-FF emulsion chains increased the infrared in mid-IR region causing increase in the –CH_2 bond vibration [36,55].

As seen in Fig. 8 (c & d), the curve was fitted to the observed variation in absorbance caused by the variation in the PEG-C-GM-FF emulsion chains density at specified radial locations using the Gaussian model in the Origin ® software. The curve fitted of the absorbance data derived from Fig. 8(a) and (b) follows a half-normal distribution. The variation in IR absorbance follows the similar distribution as the IntDen distribution of the PEG-C-GM-FF emulsion chains. The remainder of the data are presented in Fig. S7. The FTIR and image of the radial locations on the film taken at the same spot by micrometre stage.

After peakwise Gaussian curve fitting using Origin ®, the FWHM values from Fig. S7 were extracted and plotted against spinning speed to represent distribution of intensity of the 2927 cm^{-1} absorbance peak in relation to spinning speed (Fig. S8). As seen in Fig. S8, the least FWHM value for 2927 cm^{-1} peak intensity distribution for various radial locations was observed for lowest viscosity of PVA solution and at highest spinning speed. Spinning the low viscosity solution at high speed caused most of nanoemulsion droplets to remain at the centre of the substrate where the magnet was located while rest of the nanoemulsion droplets moved out of the substrate due to high inertia [22]. As seen in Fig. 8 (c)&(d), higher density of the PEG-C-GM-FF emulsion chains at the centre of the film corresponds to high intensity of the 2927 cm^{-1} absorbance
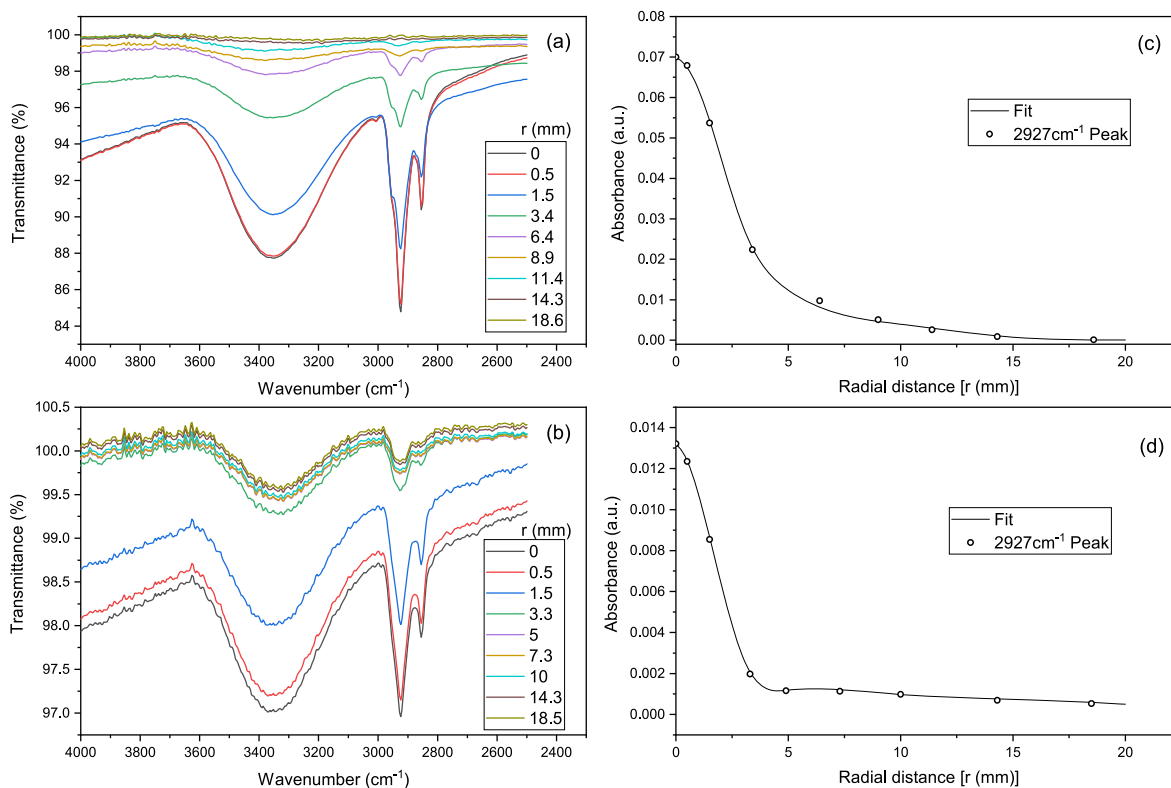
Fig. 8. FTIR absorption spectra acquired at various radial points on the thin films prepared by spinning the PEG-C-GM-FF nanoemulsion dispersed in PVA solution having 1.9 mPas viscosity (a) at 700 rpm (b) at 2500 rpm. The variation in values of the intensity of 2927 cm^{-1} peaks in relation to various radial locations extracted from the (c) spectra in (a) and (d) spectra in the (b). The fitted curve to the peak intensity data in (c) and (d) follow the half -normal distribution. Rest of the data and plots are in the (supplementary information **S.3**).
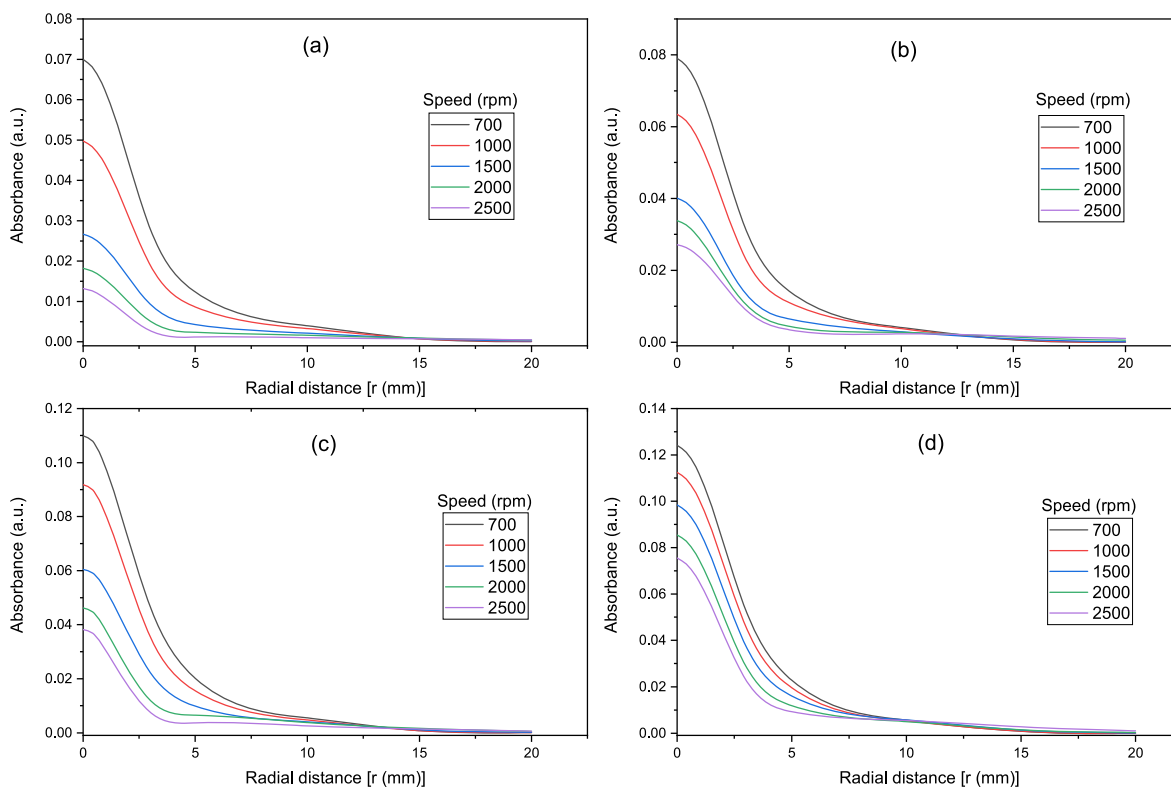
Fig. 9. Spatial half-normal IR absorption intensity distribution at various radial locations on the surface of the film prepared at different viscosities and coating speed.

peak but the intensity drops to lowest at just 5 mm away from the centre of the film. This showed that the FWHM of spatial distribution at low viscosity and high spinning speed is low which reflects in Fig. 9.

Similarly, Fig. 9 shows the distribution of the FWHM of the spatial distribution of 2927 cm^{-1} peak intensity at various radial locations. Furthermore, the relationship of FWHM of the spatial distribution of 2927 cm^{-1} peak intensity with the spin speeds (rpm) for each of the aqueous PVA viscosities shown in Fig. S8. The relationship correlates the processing parameters with the outcome in terms of the increased spatial distribution of the absorbance, which can be useful in preparing such film for enhance absorbance and detection of the low concentration molecules.

3.4. Correlation between chain density and FTIR absorption

The Full width half maximum (FWHM) of the FTIR (FTIR-FWHM) absorption at 2927 cm^{-1} for all distributions in Fig. S8 were related with the FWHM from image analysis (Image-FWHM) (Fig. 6). The relation between FWHM values was found to be linear (Fig. 10).

This trend indicated the enhancement of the –CH$_2$ signal due to its interaction with the Fe$_3$O$_4$-gold heterodimer interface. The relative change in absorbance intensities measured at the centre of the thin film and farthest zones reveal the impact of chain density and the proximity of nanoemulsion droplets that created increased surface area contact per molecule of the PVA; wherefore, the local intensities across the numerous contact sites are amalgamated into an overall boost in signal. This scenario is.

Specifically noticeable at the lower end of the plot spectrum (Fig. 10), where the PEG-C-GM-FF emulsion chains density between 0 mm ≤ r ≤ 2 mm of Fig. 5 with speed 2500 rpm, showed to be relatively higher than the rest of the zones where less density of chain and randomly dispersed. The range of FTIR-FWHM (0–~3.6 mm) for PEG-C-GM-FF emulsion chains density reveals the uniformity of the droplet chains within the film while the FTIR absorption within this range revealed a broader signal response (meaning a broad range of the wavenumbers) across the thinner films (lower PEG-C-GM-FF droplet FWHM). However, beyond the PEG-C-GM-FF emulsion chains distribution (FTIR-FWHM >3.6 mm), the hierarchical build of PEG-C-GM-FF droplet columns close to the centre of the thin film contributes excessively more to FTIR absorption intensity in relation to the other scanned zones of the thin film. Therefore, the lower the speed, the higher the viscosities, lead to thicker films which contains more columns at the centre of the film, that results to enhanced infrared absorption from the layered PEG-C-GM-FF. The broader droplet distribution coinciding with FWHM>3.6 increases IR absorption at large range of wavenumbers where FTIR-FWHM is also larger than 3.6 mm. This phenomenon can be explained by the high IR absorption at the centre due to larger surface areas exposure between the tight arrays of chains in the films. The density of PEG-C-GM-FF emulsion chains decreases with increase in the spinning speeds and decreasing viscosities due to rise in aqueous fluid velocity along increasing radial distances from the centre of the rotating substrate. The density distribution peaks of PEF-C-GM-FF emulsion chains (Fig. 5) and FTIR absorption peaks (Fig. 9) demonstrated that the absorption increases with increase in the density of the array of chain probably due to reduced gaps between chain and more hierarchical layers.

The less viscous solution (i.e.1.9 mPas) processed at speeds 2000 rpm resulted in dense chain formation within the area encompassed by radial ring (equivalent to ROI-1 to 3) at 2 mm. Outside this range revealed patches and scanty dispersions of PEF-C-GM-FF emulsion chains (see *supplementary S.2.3* for more random images). It was observed because of low polymer content within the aqueous solvent leading to the contraction of polymer film and poor coverage [62].

For viscous solution at low speeds, the viscous resistance poses lesser inertia and therefore lower degree of displacement than other lesser viscosities. The distribution is seen to be higher than others but with uniformly dense clusters having low degree of distribution between
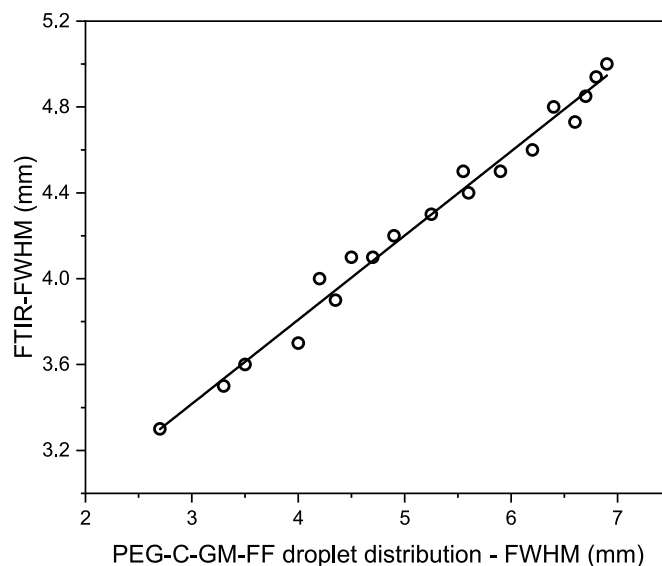

Fig. 10. Relation between the FWHM of the intensity distributions of FTIR-absorption peak at 2927 cm^{-1} and FWHM of the spatial integrated density distribution of the PEF-C-GM-FF nanoemulsion droplets.

droplets and background. Also, lower speeds resulted in film unable to dry, especially at 700 rpm. This was noticed, when the substrate and coating were removed from the magnetic setup, the superparamagnetic nature of the pickering droplet system and thermal initiated instability caused droplet chains to dissociate, and the natural drying of the film led to disordered array formation. The rate of evaporation is directly proportional to square root of spin speed, with lesser concertation of solute being higher than that of higher concentrations in the solution of polystyrene and polymethylmethacrylate in toluene [63]. This makes higher spin speeds from 1000 rpm and above for the 60 s operation time vital for sufficient water evaporation and skin formation of drying polymer [55, 56].

4. Conclusion

The magnetically directed self-assembly manufacturing technique was successfully applied by combining the magnetic field and spin coating to form the thin film with nanostructure with array of chains of the gold Pickering ferrofluid (oil based) nanoemulsion dispersed in PVA aqueous solution. The manipulation of PVA carrier phase viscosity and spin speed allowed the control of the density of gold Pickering ferrofluid (oil based) nanoemulsion chain arrays. Spinning of the emulsion with low carrier phase viscosity at high spinning speed led to a narrower PEF-C-GM-FF emulsion chains density distribution. The spinning speed has inverse relationship with the PEF-C-GM-FF emulsion chains distribution. The FTIR spectra obtained at various radial location on the film showed that the spatial distribution of CH$_2$ asymmetric (2927 cm^{-1}) absorption band intensity was linearly related to the spatial distribution of PEF-C-GM-FF emulsion chains density. Enhanced local intensity increased the PVA molecule vibration signal significantly. The magnetic and spin coating self-assembly is seen to be an easy, quick, and flexible method for creating thin film array-type patterned structure, with a tuneable and expandable throughput that depends on the areal magnetic field distribution across the substrate. It is essential to point out that the individual chains are not continuous, and possess rough edges, which is potentially not an ideal morphological feature of the film structures designed for photonic applications. However, the rough edges can provide dense local charge concentrations that lead to an enhancement in vibrational signal of analyte molecules. Overall, future work regarding optical studies on charge dynamics of the gold-iron oxide heterostructure system is imperative, as well as further improvement on array structure through

the manipulation of permanent magnets to establish properly linked magnetic fields across the substrate. Use of superparamagnetic materials and its dispersion in polymer will allow creating polymer sensor film [64, 65].

Declaration of competing interest

The authors declare that they have no known competing financial interests or personal relationships that could have appeared to influence the work reported in this paper.

Acknowledgement

Appendix A. Supplementary data

Supplementary data to this article can be found online at https ://doi.org/10.1016/j.hybadv.2023.100018.

References

[1] A. Barhoum, Garcia-Betancourt, Physicochemical Characterization of Nanomaterials: Size, Morphology, Optical, Magnetic, and Electrical Properties. Emerging Applications of Nanoparticles and Architecture Nanostructures in: Current Aspects and Future Trends Micro and Nano Technologies, Elsevier, 2018, pp. 279–304.

[2] G. Whitesides, J. Kriebel, B. Mayers, Self-assembly and nanostructured materials, in: Nanoscale Assembly, Springer, Boston, MA, 2005, pp. 217–239.

[3] A. Biswas, I.S. Bayer, A.S. Biris, T. Wang, E. Dervishi, F. Faupel, Advances in top–down and bottom–up surface nanofabrication: techniques, applications and future prospects, Adv. Colloid Interface Sci. 170 (2012) 2–27.

[4] E. Rabani, D.R. Reichman, P.L. Geissler, L.E. Brus, Drying-mediated self-assembly of nanoparticles, Nature 426 (2003) 271–274.

[5] X. Chen, S. Lenhert, M. Hirtz, N. Lu, H. Fuchs, L. Chi, Langmuir–Blodgett patterning: a bottom–up way to build mesostructures over large areas, Acc. Chem. Res. 40 (6) (2007) 393–401.

[6] K. Pancholi, P.K. Robertson, P. Okpozo, N.S. Beattie, D. Huo, Observation of stimulated emission from Rhodamine 6G-polymer aggregate adsorbed at foam interfaces, J. Phys.: Energy 1 (1) (2018), 015007;
(a) J. Fiabane, P. Prentice, K. Pancholi, High Yielding Microbubble Production Method, BioMed research international, 2016, https://doi.org/10.1155/2016/3572827. Article ID 3572827 |.

[7] Q. Zhou, P. Dong, L. Liu, C. Bingying, Study on the sedimentation self-assembly of colloidal SiO2 particles under gravitational field, Colloids Surf. A Physicochem. Eng. Asp. 253 (1–3) (2005) 169–174.

[8] M. Manstrangeli, W. Ruythooren, C. Van Hoof, J.-P. Celis, Conformal dip-coating of patterned surfaces for capillary die-to-substrate self-assembly, J. Micromech. Microeng. 19 (2009), 045015.

[9] D. Xia, A. Biswas, D. Li, S.R.J. Brueck, Directed self-assembly of silica nanoparticles into nanometer-scale patterned surfaces using spin-coating, Adv. Mater. Commun. 16 (16) (2004) 1427–1432.

[10] V. Brisson, R.D. Tilton, Self-Assembly and two-dimensional patterning of cell arrays by electrophoretic deposition, Biotechnol. Bioeng. 77 (3) (2002) 290–295.

[11] J. Fiabane, P. Prentice, K. Pancholi, High yielding microbubble production method, BioMed Res. Int. (2016), 3572827, https://doi.org/10.1155/2016/3572827 (2016). 2016.

[12] E.S. Tsurko, P. Feicht, F. Nehm, K. Ament, S. Rosenfeldt, I. Pietsch, K. Roschmann, H. Kalo, J. Breu, Large scale self-assembly of smectic nanocomposite films by doctor blading versus spray coating: impact of crystal quality on barrier properties, Macromolecules 50 (11) (2017) 4344–4350.

[13] B.P. Binks, Particles as surfactants - similarities and differences, Curr. Opin. Colloid Interface Sci. 7 (1–2) (2002) 21–41.

[14] B.P. Binks, T.S. Hozorov, Colloidal Particles at Liquid Interfaces, Cambridge University Press, Cambridge, 2006.

[15] A.P. Sommer, M. Ben-Moshe, S. Magdassi, Size-discriminative self-assembly of nanospheres in evaporating drops, J. Phys. Chem. B 108 (1) (2004) 8–10.

[16] N.J. Suematsu, Y. Ogawa, Y. Yamamoto, T. Yamaguchi, Dewetting self-assembly of nanoparticles into hexagonal array of nanorings, J. Colloid Interface Sci. 310 (2) (2007) 648–652.

[17] P.Y. Su, J.C. Hu, S.L. Cheng, L.J. Chen, J.M. Liang, Self-assembled hexagonal Au particle networks on silicon from Au nanoparticle solution, Appl. Phys. Lett. 84 (18) (2004) 3480–3482.

[18] A. Mihi, M. Ocaña, H. Míguez, Oriented colloidal-crystal thin films by spin-coating microspheres dispersed in volatile media, Adv. Mater. 18 (17) (2006) 2244–2249.

[19] M. Pichumani, P. Bagheri, K.M. Poduska, W. González-Viñas, A. Yethiraj, Dynamics, crystallization and structures in colloid spin coating, Soft Matter 9 (12) (2013) 3220–3229.

[20] G.A. Ozin, S.M. Yang, The race for the photonic chip: colloidal crystal assembly in silicon wafers, Adv. Funct. Mater. 11 (2) (2001) 95–104.

[21] M. Banik, R. Mukherjee, Fabrication of ordered 2D colloidal crystals on flat and patterned substrates by spin coating, ACS Omega 3 (10) (2018) 13422–13432.

[22] A.P. Bartlett, M. Pichumani, M. Giuliani, W. González– Viñas, A. Yethiraj, Modified spin-coating technique to achieve directional colloidal crystallization, Langmuir 28 (6) (2012) 307–3070.

[23] A. Mourkas, A. Zarlaha, N. Kourkoumelis, I. Panagiotopoulos, Self-assembly magnetic micro and nanospheres and the effect of applied magnetic fields, Nanomaterials 11 (4) (2021) 1030.

[24] R. Aslam, W. Gonzalez-Vinas, Spin coating of moderately concentrated superparamagnetic colloids in different magnetic field configuration, Physicochem. Eng. Aspects 532 (2017) 530–534.

[25] R. Aslam, W. Gonzalez-Vinas, Pattern formation in spin-coating of hybrid colloids in different magnetic field configurations, J. Phys. Appl. Phys. 52 (2019), 344001.

[26] R. Aslam, K. Shahrivar, J. de Vicente, W. Gonzalez-Vinas, Magnetorheology of hybrid colloids obtained by spin coating and classical rheometry, Smart Mater. Struct. 25 (7) (2016), 075036;
(a) S. Samal, O. Kosjakova, Surface feature of PMMA films on NiTi alloy substrate by the spin coating method, Ceram. Int. (2022), https://doi.org/10.1016/j.ceramint.2022.10.152.

[27] M. Pichumani, W. Gonzalez-Vinas, Spin -coating of dilute magnetic colloids in a magnetic field, Magnetohydrodynamics 47 (2) (2011) 191–199.

[28] M. Pichumani, W. Gonzalez-Vinas, Magnetoheology from surface coverage of spin-coated colloidal films, Soft Matter 9 (2013) 2506–2511.

[29] M. Ohring, Magnetic Properties of Materials. Engineering Materials Science, Elsevier, 1995, pp. 711–746.

[30] J. Philip, Magnetic nanofluids: recent advances, applications, challenges, and future directions, Adv. Colloid Interface Sci. (2022), 102810.

[31] S. Sachdev, R. Maugi, C. Kirk, Z. Zhou, S. Chritie, M. Platt, Synthesis and assembly of gold and iron oxide particles within an emulsion droplet; facile production of Core@shell particles, Colloid. Interf. Sci. Comm. 16 (2016) 14–18.

[32] R. Kumar, A.P. Singh, A. Kapoor, K.N. Tripathi, Fabrication and characterization of polyvinyl-alcohol-based thin-film optical waveguides, Opt. Eng. 43 (9) (2004) 2134–2142.

[33] L. Xiao, E. Yeung, Optical imaging of individual plasmonic nanoparticles in biological samples, Annu. Rev. Anal. Chem. 7 (2014) 89–111.

[34] T. Nguyen, F. Mammeri, S. Ammar, Iron oxide and gold mased magneto-plasmonic nanostructures for medical applications: a review, Nanomaterials 8 (149) (2018) 1–29.

[35] G.I. Dovbeshko, V.I. Chegel, N.Y. Gridina, O.P. Repnytska, Y.M. Shirshov, V.P. Tryndiak, G.I. Solyanik, Surface enhanced IR absorption of nucleic acids from tumor cells: FTIR reflectance study, Biopolymers: Orig. Res. Biomol. 67 (6) (2002) 470–486.

[36] T. Maß, V. Nguyen, U. Schnakenberg, T. Taubner, Tailoring grating strip widths for optimizing infrared absorption signals of an adsorbed molecular monolayer, Opt Express 27 (8) (2019) 10524–10532.

[37] K. Ataka, J. Heberle, Biochemical applications of surface-enhanced infrared absorption spectroscopy, Anal. Bioanal. Chem. 388 (1) (2007) 47–54.

[38] C. Lai, F. Low, M. Tai, S. Abdul-Hamid, Iron oxide nanoparticles decorated Oleic acid for high colloidal stability, Adv. Polym. Technol. 37 (6) (2017) 1712–1721.

[39] R.E. Rosensweig, Dover Publications, Inc., Ferrohydrodynamics, New York, 1985.

[40] B. Patricia, N. Adelman, J.B. Katie, J.C. Dean, B.E. Arthur, C.L. George, Preparation and properties of an aqueous ferrofluid, J. Chem. Educ. 76 (7) (1999) 943–948.

[41] E.T. Roe, J.T. Scanlan, D. Swern, Fatty acid amides. I. Preparation of amides of oleic and the 9, 10-dihydroxystearic acids, J. Am. Chem. Soc. 71 (6) (1949) 2215–2218.

[42] I. Hussain, M. Brust, A.J. Papworth, A.I. Cooper, Preparation of acrylate-stabilized gold and silver hydrosols and gold-polymer composite films, Langmuir 19 (11) (2003) 4831–4835.

[43] M. Deng, N. Tu, F. Bai, L. Wang, Surface functionalization of hydrophobic nanocrystals with one particle per micelle for bioapplications, Chem. Mater. 24 (13) (2012) 2592–2597.

[44] A. Escudero, A.I. Becerro, C. Carillo-Carrion, N.O. Nunez, M.V. Zyuzin, M. Laguna, D. Gonzalez-Manebo, M. Ocana, W.J. Parak, Rare earth based nanostructured materials: synthesis functionalization, properties and bioimaging and biosensing applications, Nanophotonics 6 (5) (2017) 881–921;
(a) J. Philip, T. Jaykumar, P. Kalyanasundaram, B. Raj, O. Mondain-Monval, Effect of polymer-surfactant association on colloidal force, Phys. Rev. 66 (1) (2002), 011406;
(b) D.K. Mohapatra, J. Philip, Effect of surface charge screening on critical magnetic fields during field induced structural transitions in magnetic fluids, J. Appl. Phys. 125 (24) (2019), 244301;
(c) J. Philip, G.G. Prakash, T. Jaykumar, P. Kalyanasundaram, O. Mondain-Monval, B. Raj, Interaction between emulsion droplets in the presence of polymer– surfactant complexes, Langmuir 18 (12) (2002) 4625–4631;
(d) T. Muthukumaran, J. Philip, Synthesis of water dispersible phosphate capped CoFe2O4 nanoparticles and its applications in efficient organic dye removal, Colloids Surf. A Physicochem. Eng. Asp. 610 (2021), 125755.

[45] C. Bunn, Crystal structure of polyvinyl alcohol, Nature 161 (4102) (1948) 929–930.

[46] P. Byron, R. Dalby, Effects of heat treatment on the permeability of polyvinyl alcohol films to a hydrophilic solute, J. Pharmaceut. Sci. 76 (1) (1987) 65–67.

[47] Y. Lo, Y. Chiu, H. Tseng, J. Chen, Thermal-annealing-induced self-stretching: fabrication of anisotropic polymer particles on polymer films, Langmuir 33 (43) (2017) 12300–12305.

[48] M. Kozlov, Ultra-Thin Films of Polyvinyl Alcohol on Hydrophobic Surfaces: Preparation, Properties, Chemistry, and Applications, PhD Dissertation, University of Massachusetts Amherst., Massachusetts, 2004.

[49] J. Chalmers, Handbook of Vibrational Spectroscopy, second ed., Wiley & Sons, 2002 l.

[50] L. Ng, R. Simmons, Infrared spectroscopy, Anal. Chem. 71 (12) (1999) 343–350.

[51] C. Russo, F. Stanzione, A. Tregrossi, A. Ciajolo, Infrared spectroscopy of some carbon-based materials relevant in combustion: qualitative and quantitative analysis of hydrogen, Carbon 74 (2014) 127–138.

[52] D. Hashim, Y.C. Man, R. Norakasha, M. Shuhaimi, Y. Salmah, Z.A. Syahariza, Potential use of Fourier transform infrared spectroscopy for differentiation of bovine and porcine gelatins, Food Chem. 118 (3) (2010) 856–860.

[53] R. Adato, A.A. Yanik, J.J. Amsden, D.L. Kaplan, F.G. Omenetto, M.K. Hong, S. Erramilli, H. Altug, Ultra-sensitive vibrational spectroscopy of protein monolayers with plasmonic nanoantenna arrays, Proc. Natl. Acad. Sci. USA 106 (46) (2009) 19227–19232.

[54] T. Mayerhöfer, J. Popp, Periodic array-based substrates for surface-enhanced infrared spectroscopy, Nanophotonics 7 (1) (2018) 39–79.

[55] C. Huck, F. Neubrech, J. Vogt, A. Toma, D. Gerbert, J. Katzmann, T. Härtling, A. Pucci, Surface-enhanced infrared spectroscopy using nanometer-sized gaps, ACS Nano 8 (5) (2014) 4908–4914.

[56] E. Blout, R. Karplus, The infrared spectrum of polyvinyl alcohol, J. Am. Chem. Soc. 70 (2) (1948) 862–864.

[57] A. Wexler, Integrated intensities of absorption bands in infrared spectroscopy, Appl. Spectrosc. Rev. 1 (1) (1967) 29–98.

[58] R. Fogel, M.J. Rutherford, The solubility of carbon dioxide in rhoyolitic melts; quantitative FTIR study, Am. Minerologist. 75 (11–12) (1990) 1311–1326.

[59] D. Finlayson, C. Rinaldi, C.M. Baker, Is infrared spectroscopy ready for the clinic? Anal. Chem. 91 (19) (2019) 12117–12128.

[60] M. Pilling, P. Gardner, Fundamental developments in infrared spectroscopic imaging for biomedical applications, Chem. Soc. Rev. 45 (7) (2016) 1935–1957.

[61] I.L. Larsen, Slide rule conversion of percent transmittance to absorbance, J. Chem. Educ. 48 (6) (1971) 388.

[62] M.H. Mondal, M. Mukherjee, K. Kawashima, K. Nishida, T. Kanaya, Study of thickness dependent density in ultrathin water-soluble polymer films, Macromolecules 42 (3) (2009) 732–736.

[63] J. Danglad-Flores, S. Eickelmann, H. Reigler, Evaporation behaviour of a thinning liquid film in a spin coating setup: comparison between calculation and experiment, Eng. Rep. 3 (9) (2021), 12390. Wiley.

[64] R. Gupta, P. Gupta, C. Footer, G.B. Stenning, J.A. Darr, K. Pancholi, Tuneable magnetic nanocomposites for remote self-healing, Sci. Rep. 12 (2022), 10180, https://doi.org/10.1038/s41598-022-14135-8.

[65] S. Samal, O. Kosjakova, D. Vokoun, I. Stachiv, Shape memory behaviour of PMMA-coated NiTi alloy under thermal cycle, Polymers 14 (14) (2022) 2932.

Study of Spatial Organisation of Magnetic Field Directed Gold-Pickering-Ferrofluid-Nanoemulsion in Spin Coated Film

Paul Okpozo[1], Ketan Pancholi[1,2]*

[1]School of Engineering, Robert Gordon University, Aberdeen AB10 7GJ, United Kingdom
[2]Advanced Materials Group, School of Engineering, Robert Gordon University, Aberdeen, AB10 7GJ, United Kingdom
*Corresponding author:k.pancholi2@rgu.ac.uk

S.1) Pickering Emulsion characterisation

S. 1.1) Photo and TEM images of prepared magnetite and gold methacrylate
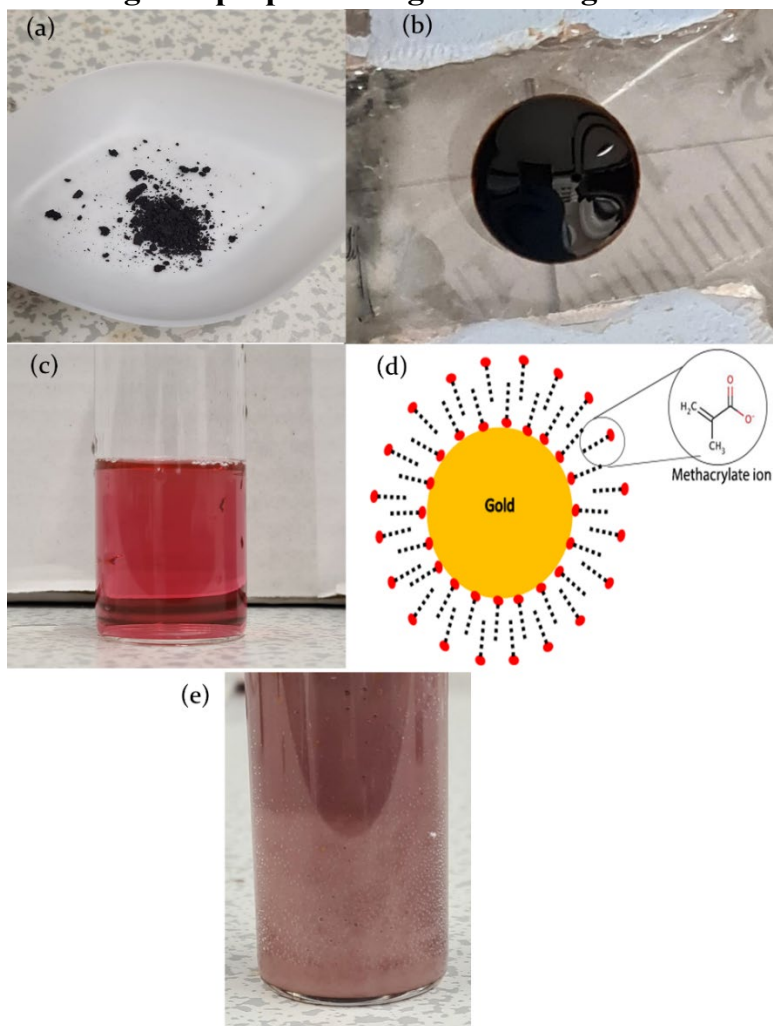
Figure S1: Photo-images of (a) dried Oleic coated Fe₃O₄ particles (OCM), (b) OCM dispersed in Cis-Cyclo-Octene (ferrofluid), (c) Gold - methacrylate colloidal dispersion, (d) Illustration of methacrylate ion interaction with gold nanoparticle, (e) Gold pickering – ferrofluid emulsion (PEG-C-GM-FF).

5 μL of magnetite colloid solution and PEG-C-GM solution was deposited on TEM grids and allowed to dry under vacuum (8 Pa) at 20°C. As for the pickering droplet in water solution, a microscopic slide was mechanically etched using a hand drill to contain and hold the TEM carbon film copper made grid. The solution was spin-coated over the grid and glass slide. The grid was removed and no further action was taken prior to the electron microscope scan. The equipment used was the JEOL® 1200TEM – 80kV accelerating voltage for the image capturing.

Figure S2 (a and b) reveals the TEM images of Fe_3O_4 and gold methacrylate. The nanoparticles diameter were measured manually using line tool drawn across each particle sample in Image J® and histogram distribution of sample sizes were plotted using Origin® software. The statistical mean and standard deviations were also determined. The histogram distribution plots for each colloid type were placed beneath the respective colloid images. Figure S2 shows an image of a dried ferrofluid droplet Pickering with gold nanoparticles.
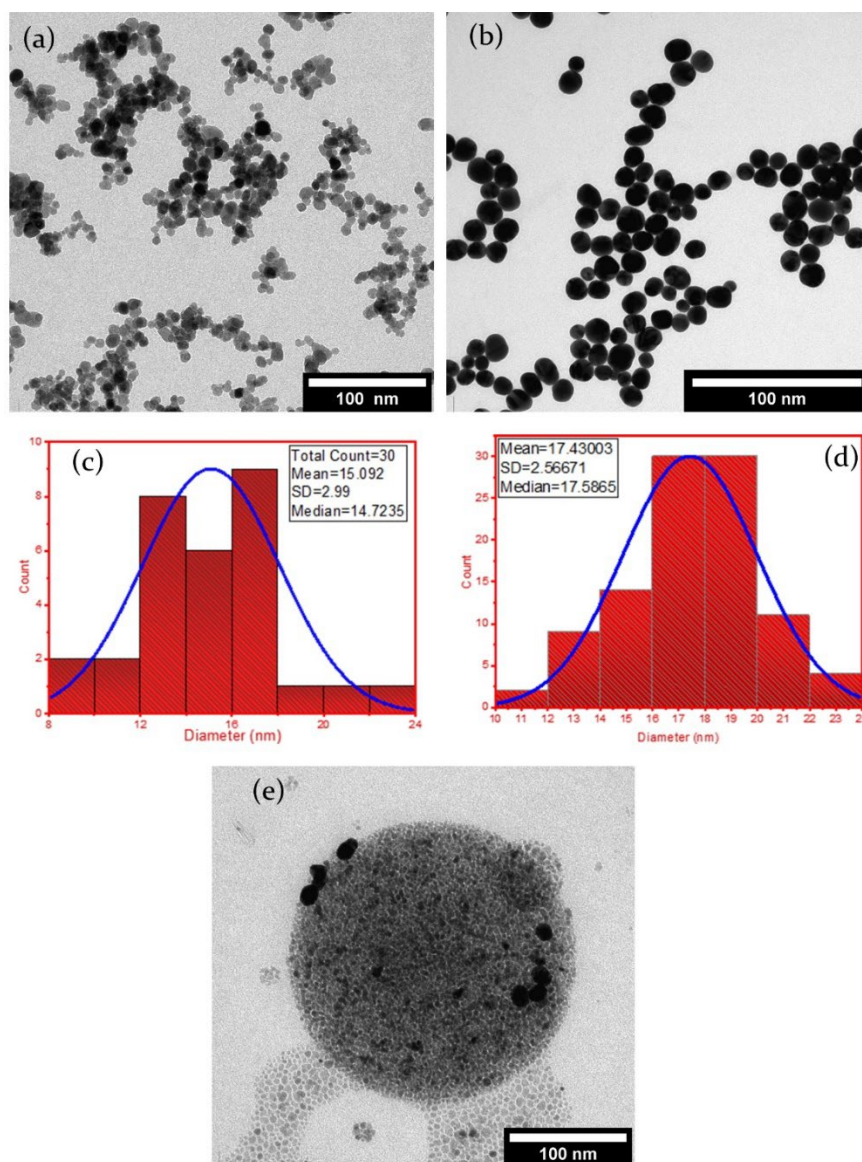
Figure S2: TEM images of (a) Fe₃O₄, (b) gold-Methacrylate. Particle size distribution histogram with measurements taken from TEM images (a & b) of (c) Fe₃O₄ and (d) Gold methacrylate, (e) dried PEG-C-GM-FF with majority of PEG-C-GM dislodged due to evaporated/drained cis-cyclooctene.

S. 1.2) Magnetic Hysteresis of Fe₃O₄ and OCM

The magnetometer device (SQUID) that measures extremely subtle magnetic fields as low as 5×10^{-14} Tesla. 1g each of the samples were tested at 300K. The test generated M-H (magnetic moment vs magnetic field) curves
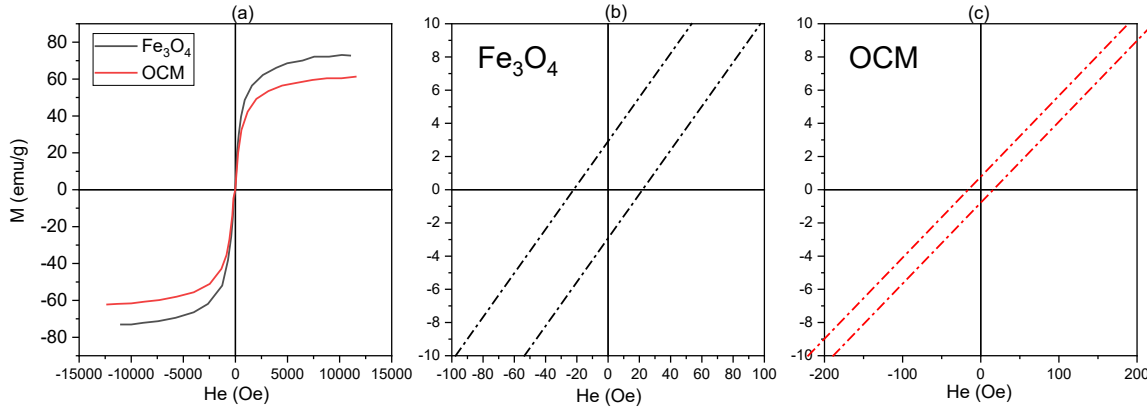
Figure S3: SQUID measurements taken at 300K for magnetic hysteresis curve generation of (a)Fe₃O₄ and OCM. (b) and (c) shown the magnified range of the hysteresis curve to obtain coercivity (H_o) for both magnetite and OCM materials respectively

The M_d for Fe₃O₄ nanoparticle is 446 kA/m. the saturation of magnetisation M_s for Fe₃O₄ and OCM are 374.755 kA/m and 219.906 kA/m respectively The magnetic susceptibility X_{iL}, which is the initial slope of the curve coinciding at H=0 for Fe₃O₄ and OCM are 8.567 and 1.54 respectively. The coercivity of Fe₃O₄ nanoparticles and OCM from Figure 3-7(b &c) are 1.753 kA/m and 1.275 kA/m respectively. The obtained experiment data were used to determine effective diameter and standard deviation of tested materials using model generated by Chantrell and co. [1, 2] (see equations S1 & S2)

$$D_m = \left\{ \left[\frac{18KT}{\pi M_d \mu_o} \right] \times \sqrt{\left[\frac{\chi_{iL}}{3 M_s H_o} \right]} \right\}^{1/3} \tag{S1}$$

$$\sigma_m = \sqrt{\ln(3\chi_i H_o)} \tag{S2}$$

$$\chi_i = \frac{\chi_{iL}}{1 + \frac{1}{3}\chi_{iL}} \tag{S3}$$

Where,

M_d is the saturation of magnetization of bulk material, χ_{iL} is the initial susceptibility from magnetization of test sample, χ_i *is the reduced initial susceptibility*, M_s is saturation magnetization of test sample, H_o is the coercivity of the test material, μ_o is the is free space magnetic permeability, given as $4\pi \times 10^{-7}$ N/A².

Table S1 Summary of results from magnetic hysteresis to obtain diameter and standard deviation of samples.

Material	Density (Kg/m^3)	X_{II}	X_I	Ms (kA/m)	Ho (kA/m)	M_d (kA/m)	D_m (nm)	σ_m
Fe$_3$O$_4$	5150	8.57	2.2	374.8	1.75	446	14.1	3.1
OCM	3640	3.16	1.5	220	1.28	446	13.7	2.9

1 Oe = 79.5575 A/m, K_B = 1.381 X 10^{-23}N.m/K, 1 emu/g = 1 Am^2/kg

The obtained sizes of samples were compared with TEM image size distribution averaging and the diameter difference between Hysteresis data and TEM for Fe$_3$O$_4$ was ~1nm irrespective of standard deviation. Meanwhile the thickness of oleic molecule layering around magnetite nanoparticles is;

(15.1 – 13.7)/2 = 0.7 nm

Upon test of OCM dissolved in Cis-Cyclooctene, the saturation of magnetization obtained was 29.5 kA/m.

S. 1.3) Dynamic Light Scattering (DLS) measurements of Gold methacrylate (GM), PEG-C-GM and PEG-C-GM-FF

DLS measurements were conducted with a Zetasizer Nano ZS instrument from Malvern at a fixed angle of 173° (backscattering detection) with a He–Ne laser (λ = 633 nm; 4 mW) and digital autocorrelator. The mean particle size was determined by a number plot. A 5 μL of prepared GM (prior to addition of PEG 40S) was dispersed in 10ml of deionized water. Out of 10 ml, the 3ml of solution was poured into a PMMA cuvette and placed into the Malvern zeta sizer Nano zs using DLS mode for scanning at 20°C operating temperature. The scanner was set to 14 runs per scan and reported value by taking cumulative average of the three scans, as it was repeated for the PEG-C-GM suspension. Size distribution of GM and OEG-C-GM measured with zeta sizer is shown in Figure S4. The average hydrodynamic size of particles for gold methacrylate was 18.63nm with standard deviation of 3.91, while PEG-C-GM gave a mean diameter of 28.8nm with standard deviation of 7.4. This meant that the PEG 40S created a coating layer of approximately 5nm.
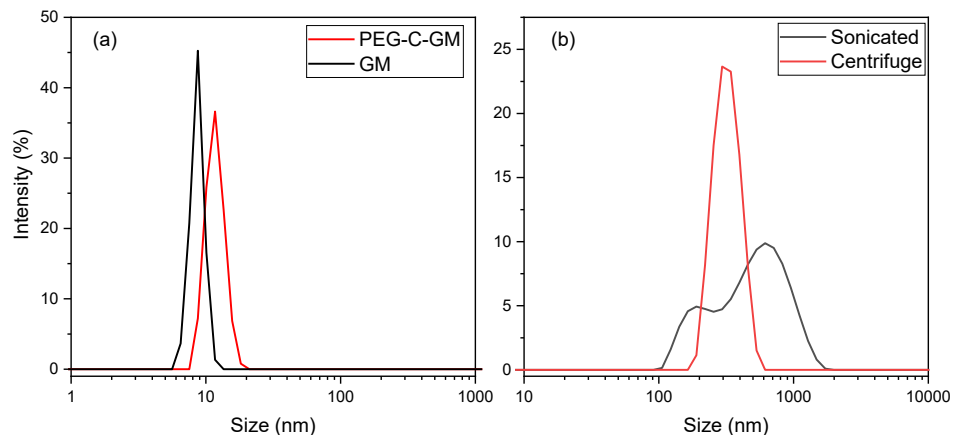
Figure S4: Zeta sizing measurements (DLS) of (a) Gold methacrylate before coating with PEG 40S (18.6nm, SD 3.9) and after coating with PEG40S (28.8nm, SD 7.4). (b) The bimodal size distribution of probe ultrasonicated PEG-C-GM-FF averaging 600 ± 500 nm (Black line), and a size management approach using centrifugation spun at 4500 rpm for 10 minutes yielding modal distribution averaging 330 ± 200 nm.

S. 1.4) Zeta Potential of Colloids and composites

This test helped in determining the charge on particle surface, and how well each stage of synthesis affected the integrity of the nanoparticles. It also helped in identifying if complex systems were stable or unstable [3]. Zeta potential measurement were conducted for PEG-C-GM-pi-FF in DI water that was injected into Malvern ® DTS1070 disposable cuvettes. 12 Zeta runs at 21°C operating temperature was the setting
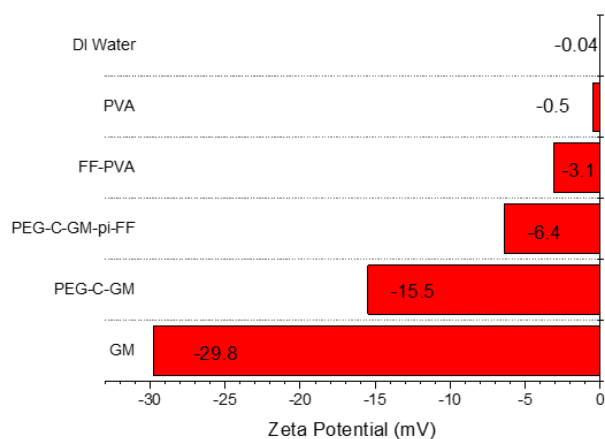
Figure S5: Zeta potential of colloids and composites

The Zeta potential results are shown in Figure S5. The overlaying of the free attached carboxylic acid led to an increased electronegative charge about each gold nanoparticle set at a high value of -29.8mV, with pH at 5.6 [4]. However, the PEG 40s coating reduced the charge due to its zwitterionic nature by acting as a form of grafting layer [5]. The gold pickering ferrofluid emulsion showed a lower electronegativity, which could be as a result of decrease of surface exposure gold nanoparticles sitting at the liquid interface or insufficient amount of PEG-C-GM around the droplet [6]. Aqueous PVA showed low electronegativity making it suitable to work with the pickering emulsion, as two electronegative charges repel, thereby eliminating the possibility of chemical bonds/linkages formed that might distort formation of droplets dipole-dipole chains upon introduction of external magnetic field.

S.2) Image Analysis

S. 2.1) Region of interest measurements for 3.5mPas at 700rpm and 2000rpm

Table S2: Region of interest pixel intensity density Measurements for 3.2mPas at 700rpm sample

Label	Radius (um)	Area	StdDev	Min	Max	IntDen	Int/Area
ROI_1	1.64E+01	8.48E+02	3.30E+02	1.00E+01	2.30E+02	3.46E+06	4.08E+03
ROI_2	4.05E+01	5.15E+03	1.40E+02	1.20E+01	2.65E+02	2.10E+07	4.08E+03
ROI_3	7.10E+01	1.58E+04	1.43E+02	1.50E+01	3.18E+02	6.45E+07	4.08E+03
ROI_4	1.11E+02	3.84E+04	1.44E+02	2.00E+01	3.33E+02	1.55E+08	4.04E+03
ROI_5	1.50E+02	7.03E+04	1.45E+02	2.00E+00	3.53E+02	2.80E+08	3.99E+03
ROI_6	2.10E+02	1.38E+05	1.46E+02	1.90E+01	3.78E+02	5.37E+08	3.89E+03

Table S3: Region of interest pixel intensity density Measurements for 3.2mPas at 2000rpm sample

Label	Radius (um)	Area	StdDev	Min	Max	IntDen	Int/Area
ROI_1	1.64E+01	8.48E+02	3.30E+02	1.00E+00	2.30E+03	1.32E+06	1.56E+03
ROI_2	4.05E+01	5.15E+03	2.71E+02	1.00E+00	2.30E+03	8.04E+06	1.56E+03
ROI_3	7.10E+01	1.58E+04	2.54E+02	1.00E+00	2.47E+03	2.47E+07	1.56E+03
ROI_4	1.11E+02	3.84E+04	2.58E+02	1.00E+00	2.55E+03	5.49E+07	1.43E+03
ROI_5	1.50E+02	7.03E+04	2.64E+02	1.00E+00	2.55E+03	9.16E+07	1.30E+03
ROI_6	2.10E+02	1.38E+05	2.57E+02	1.00E+00	2.55E+03	1.61E+08	1.17E+03

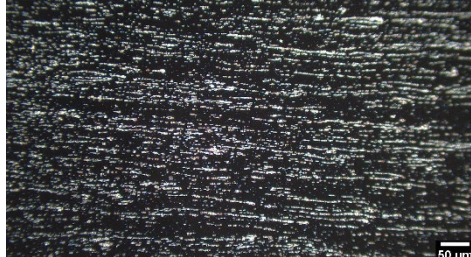## S. 2.2) Image density fitting
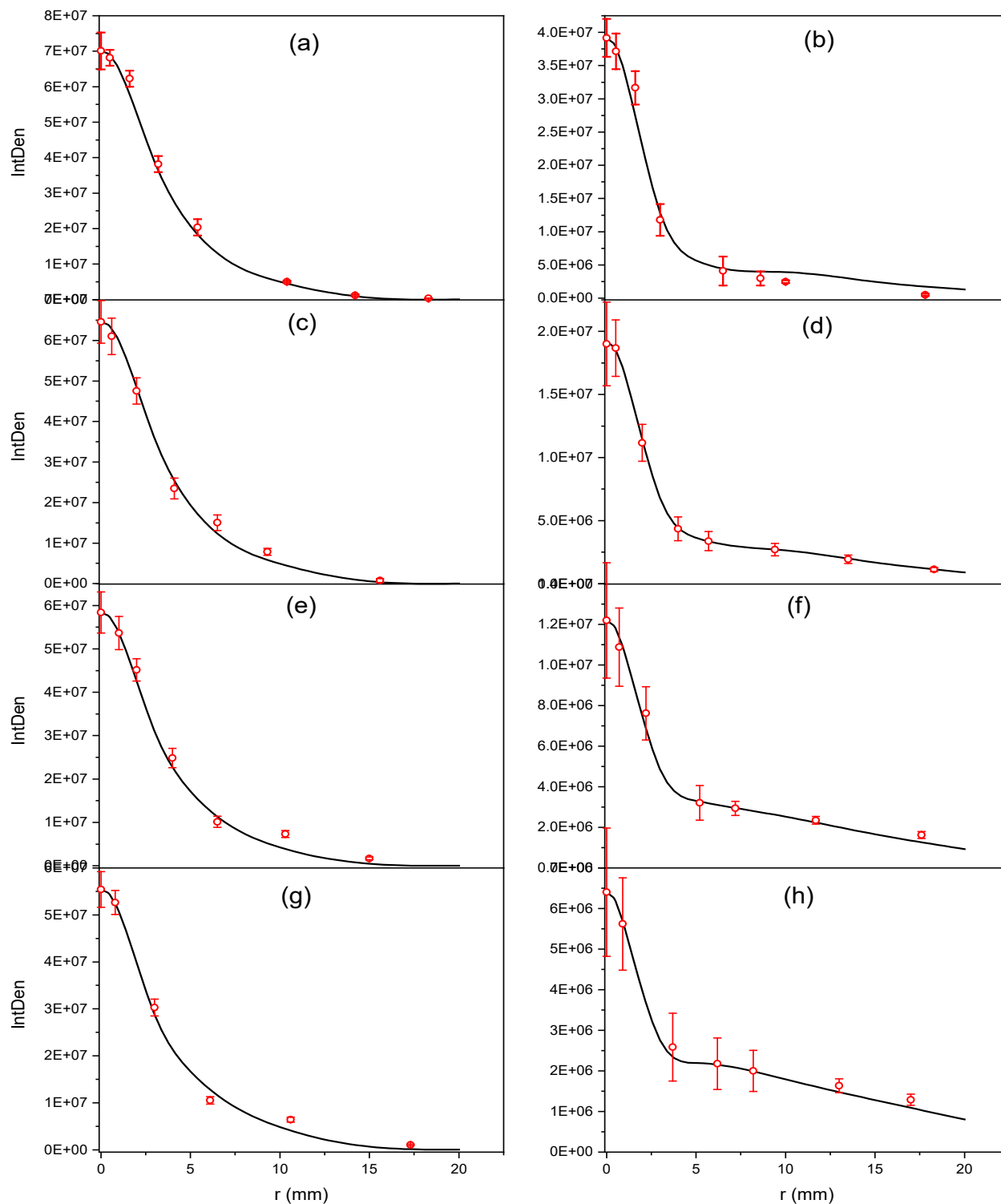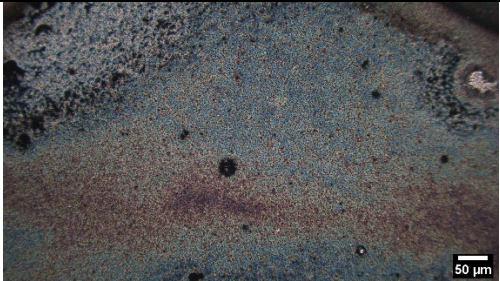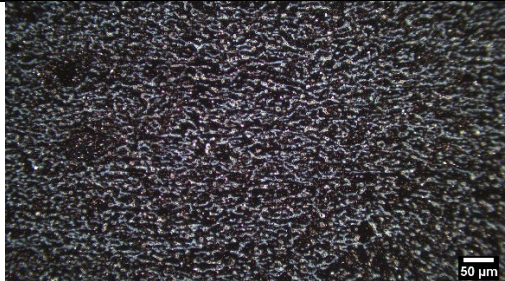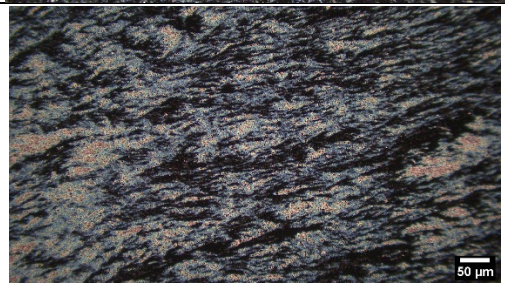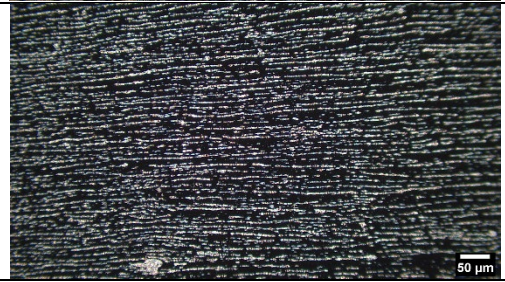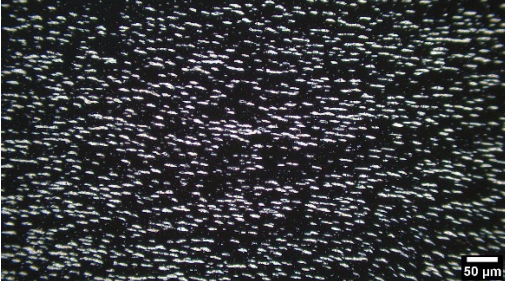
Figure S6: Fitting of data from pixel density of image analysis for (a) 43.2mPas @700rpm, (b) 43.2mPas @2500rpm (c) 15.2mPas @700rpm, (d) 15.2mPas @2500rpm, (e) 3.21mPas 700rpm, (f) 3.21mPas 2500rpm (g)1.9mPas @700rpm, and (h) 1.9mPas @2500rpm.

S. 2.3) Some images of PEG-C-GM-pi-FF in PVA prepared at different viscosities and spin speeds

Viscosity (mPas)/Speed (rpm)	R=0 mm	R= ~10 ±1.5 mm
1.9/1500		
3.2/700		
15.2/2000		
43.2/2500		
3.2/2000		

Images continued…

Viscosity (mPas)/Speed (rpm)	R=0 mm	R= ~10 ±1.5 mm
3.2/2500		
1.9/1000		

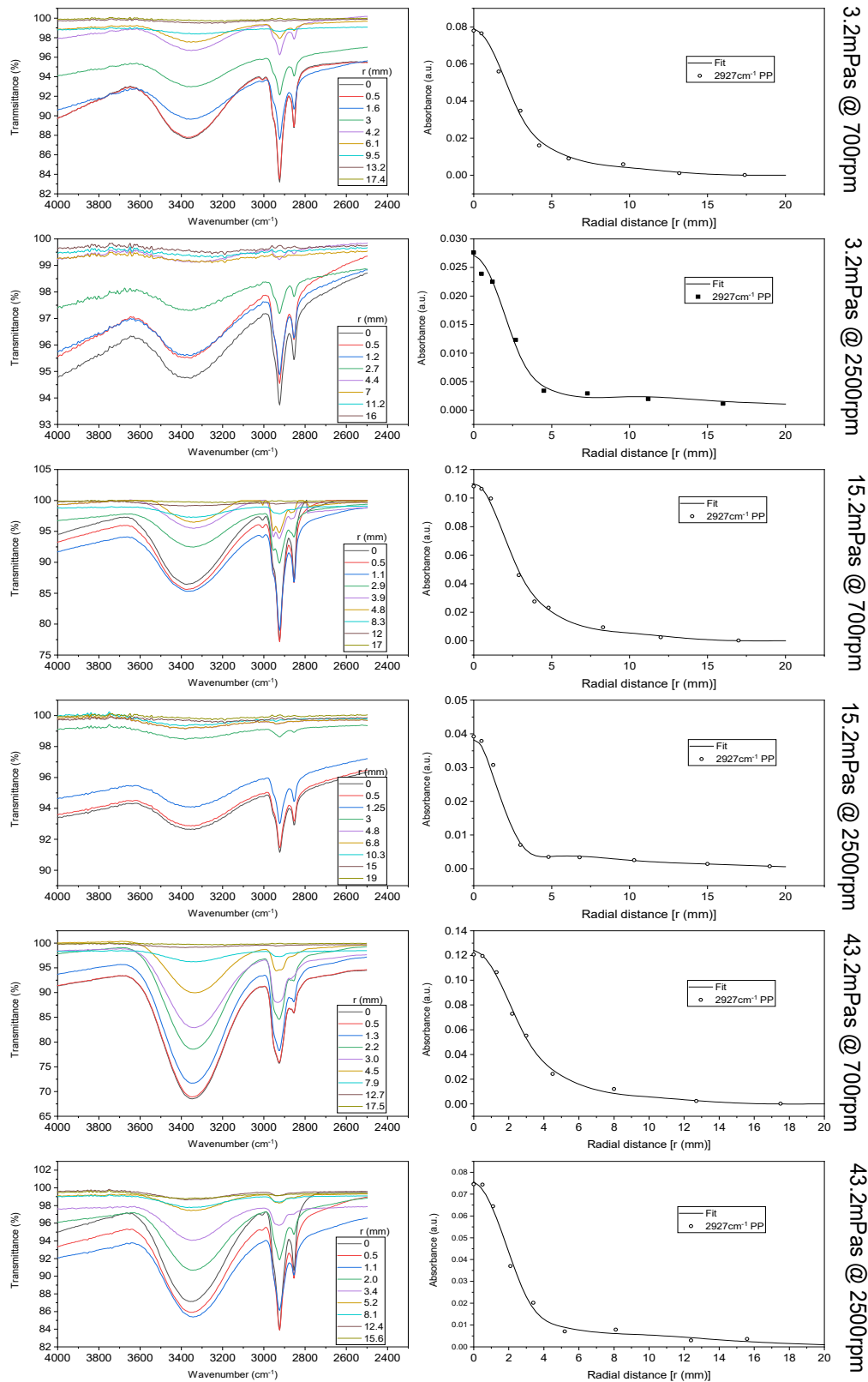## S.3) FTIR Transmission mode absorption data for thin film pattern on optical glass

Figure S7: Rest of fit 2927cm⁻¹ peak transmittance intensity converted to absorbance across radial points for each viscosities and spin speeds (3.2mPas, 15.2mPas and 43.2mPas).
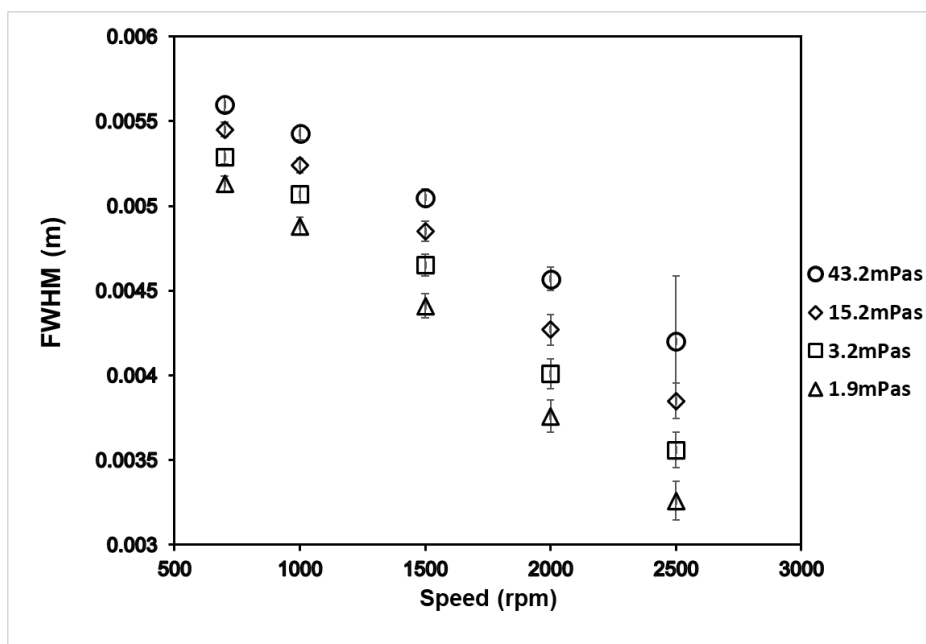
Figure S8: The full width half measure (FWHM) of absorbance peak (2927cm^{-1}) across thin film prepared with PVA viscosities (1.9 mPas, 3.2 mPas, 15.2 mPas and 43.2 mPas) plotted against spin speed (rpm).

S.4) References

1) Chantrell, R., Popplewell, J. & Charles, S., 1978. Measurements of particle size distribution parameters in ferrofluids. *IEEE Transactions on Magnetics,* 14(5), pp. 975-977.
2) Hussain, I., Brust, M., Papworth, A. J. & Cooper, A. I., 2003. Preparation of Acrylate-Stabilized Gold and Silver Hydrosols and Gold-Polymer Composite Films. *Langmuir,* 19(11), pp. 4831-4835.
3) Mourdikoudis, S., Pallares, R. & Thanh, N. T. K., 2018. Characterization techniques for nanoparticles: comparison and complementarity upon studying nanoparticle properties. *Nanoscale,* Volume 10, p. 12871.
4) O'grady, K., El-Hilo, M. & Chantrell, R., 1993. The characterisation of interaction effects in fine particle systems. *IEEE transactions on magnetics,* 29(6), pp. 2608-2613.
5) Y. Wang, J. Enrico, T. Ono, M. Maeki, M. Tokeshi, T. Isono, K. Tajima, T. Satoh, S. Sato, Y. Miura and T. Yamamoto, Enhanced dispersion stability of gold nanoparticles by the physisorption of cyclic poly (ethylene glycol). *Nature communications,* 11(1) (2020) 1-12.
6) M. Hu, X. Du, G. Liu, Y. Huang, Z. Liu, S. Sun and Y. Li, Oppositely charged Pickering emulsion co-stabilized by chitin nanoparticles and fucoidan: Influence of environmental stresses on stability and antioxidant activity. *Foods*, *11*(13), (2022) 1835.